ORNL/TM-2023/3226
CRADA/NFE-21-08844

Integrated Process and Materials Modeling for Development of Additive Manufacturing of Refractory Materials for Critical Applications

December 2023

Nithin Panicker
Bhagyashree Prabhune
Marco Delchini
Nate See
Brian Jordan
Bryan Lim
Soumya Nag
Yuri Plotnikov
Pikee Priya
Yousub Lee

CRADA FINAL REPORT
APPROVED for PUBLIC RELEASE

OAK RIDGE National Laboratory

ORNL IS MANAGED BY UT-BATTELLE LLC FOR THE US DEPARTMENT OF ENERGY

DOCUMENT AVAILABILITY

Reports produced after January 1, 1996, are generally available free via OSTI.GOV.

Website www.osti.gov

Reports produced before January 1, 1996, may be purchased by members of the public from the following source:

National Technical Information Service
5285 Port Royal Road
Springfield, VA 22161
Telephone 703-605-6000 (1-800-553-6847)
TDD 703-487-4639
Fax 703-605-6900
E-mail info@ntis.gov
Website http://classic.ntis.gov/

Reports are available to US Department of Energy (DOE) employees, DOE contractors, Energy Technology Data Exchange representatives, and International Nuclear Information System representatives from the following source:

Office of Scientific and Technical Information
PO Box 62
Oak Ridge, TN 37831
Telephone 865-576-8401
Fax 865-576-5728
E-mail reports@osti.gov
Website https://www.osti.gov/

ORNL/TM-2023/3226
CRADA/NFE-21-08844

Computational Sciences and Engineering Division

INTEGRATED PROCESS AND MATERIALS MODELING FOR DEVELOPMENT OF ADDITIVE MANUFACTURING OF REFRACTORY MATERIALS FOR CRITICAL APPLICATIONS

Author(s)

Nithin Panicker*
Bhagyashree Prabhune*
Marco Delchini*
Nate See*
Brian Jordan*
Bryan Lim*
Soumya Nag*
Yuri Plotnikov†
Pikee Priya*
Yousub Lee*

December 2023

Prepared by
OAK RIDGE NATIONAL LABORATORY
Oak Ridge, TN 37831
managed by
UT-BATTELLE LLC
for the
US DEPARTMENT OF ENERGY
under contract DE-AC05-00OR22725

---

* Oak Ridge National Laboratory
†Commonwealth Center for Advanced Manufacturing

CONTENTS

LIST OF FIGURES

LIST OF TABLES

ACKNOWLEDGEMENTS

This research was supported by the High-Performance Computing for Manufacturing Project Program (HPC4Mfg), managed by the U.S. Department of Energy Advanced Materials and Manufacturing Technologies Office (AMMTO)within the Energy Efficiency and Renewable Energy Office. This research used resources of the Compute and Data Environment for Science (CADES) at the Oak Ridge National Laboratory (ORNL), which is supported by the Office of Science of the U.S. Department of Energy under Contract No. DE-AC05-00OR22725. The authors thank to Dr. Ramanan Sankaran and Kyle Snyder, Dr. Richard P. Martukanitz, and other project team members from Siemens Corporate Technology, University of Virginia, and Virginia State University.

ABSTRACT

The research is focused on establishing computational framework, fundamental knowledge, and powder direct energy deposition (DED) capabilities for accelerating the use of refractory metals for gas turbine generation, which is considered a significant enabling technology for increasing operating temperatures and improving efficiency of these system. A computational fluid dynamics (CFD) melt pool simulation for refractory alloy of C103 was developed in Star-CCM+ by incorporating physical interactions among the heat source, material, and manufacturing parameters in multi-physics simulation. The main set of experimental data was obtained from DED trials using C103 powder at the Commonwealth Center for Advanced Manufacturing (CCAM). The modeling results, along with experimental data, were used to establish process maps for defect detection and geometric precision. The outcomes of simulations and data for C103 can be used to optimize the process parameters and tool path strategies to ensure the defect-free parts. The technology developed in the project supports the optimization of the powder DED.

1. STATEMENT OF OBJECTIVES

1.1 INTRODUCTION

Current projections for increasing the efficiency of natural gas turbine energy generation have identified the need for materials capable of prolonged operating temperatures of 1300 °C, and refractory metals are being considered for achieving this goal. Because of the high melting temperatures and difficulty in processing refractory metals through conventional ingot or casting processes, components produced using these materials have traditionally been fabricated through powder metallurgy (PM) processes [1]. Hence, the potential for using refractory metals in gas turbine energy generation is hampered by the additional cost for manufacturing these materials into product. Typically, machining of refractory materials is difficult, and mechanical properties of parts produced using PM techniques may, on occasion, suffer from inhomogeneity of composition, microstructure, and properties. A potential solution to address the increased manufacturing cost associated with refractory metals for this industry is the use of additive manufacturing (AM), which has been shown to be highly suitable for cost-effective production of complex components from high value materials at relatively low production rates. The AM processes also offer superior design flexibility, potential for weight reduction through improved design and/or part consolidation, as well as a reduction in lead time, assembly cost, and material waste. Because of the potential for these materials in applications requiring elevated temperatures, the Manufacturing Demonstration Facility (MDF) in ORNL has explored AM processing and characterization of various refractory metals, such as pure-W, pure-Mo, Mo + HfC, and Nb-alloys. Although AM improves the cost competitiveness for utilizing refractory metals, the deposition technology is not completely matured to consistently produce material having internal quality and microstructure suitable for critical applications. Because of the inherently high melting temperature of these materials, processing parameters must be closely defined and continually controlled such that the shape of the liquid pool results in consistent fusion between adjacent melt tracks and layers. The high melting temperatures may impede fusion during deposition if insufficient energy is employed, whereas excessive energy may lead to oxidation or vaporization of other species. The proper selection of energy during processing also has ramifications for generation of residual stresses, the rate of cooling through the regime that may experience ductile-brittle transition temperature (DBTT), and morphology and chemical distribution occurring during solidification. In addition, refractory metals have high affinity for interstitial species, such as oxygen, nitrogen, and hydrogen, and this can lead to formation of brittle phases and high amounts of porosity and cracking [2]. Although extremely limited data is available within the open literature, it has been shown that Ta and Nb-alloys having adequate strength and ductility can be produced using additive technology with optimum process conditions and advanced process control [3, 4].

Hence, to further extend the use of AM for refractory metals for critical applications, in particular C103 alloy, a Computational Fluid Dynamics (CFD) framework was developed within the commercial CFD code StarCCM+. A validation study was conducted to confirm accuracy of the CFD model. Postprocessing routines were developed to generate process maps. A process map was generated using the data on thermal gradients within the melt pool. The physical realizability and the range of applications of the process map generated is discussed.

1.2 BACKGROUND

Refractory metals, such as niobium (Nb), tantalum (Ta), molybdenum (Mo), and tungsten (W), and their alloys possess high melting temperatures and retain strength and hardness at elevated temperatures [1, 2]. Such properties make refractory metals and alloys suitable for applications such as aerospace propulsion (thrusters, nozzles, thrust augmenter flags) [3-5] and energy generation (nuclear reactors [6], nuclear space power, gas turbines, fusion, and light water reactors [7]). Additionally, refractory materials find applications in the biomedical sector as bio-inert materials [8-10], electronics industry as capacitors [11, 12] and superconductors [13], and in chemical process industries due to their chemical stability [14].

Conventional casting processes face challenges when processing refractory metals due to their elevated melting temperatures. Consequently, the fabrication of refractory material components necessitates cost-intensive methods such as powder metallurgy (PM) [15-17]. Hence, the potential for using refractory metals is hampered by the additional cost of manufacturing these materials into product. Moreover, the mechanical properties of parts produced using PM techniques may suffer from inhomogeneity of composition, microstructure, and properties [17]. Moreover, it is difficult to fabricate parts with complex geometries using PM [18]. Traditional subtractive manufacturing techniques, such as machining, lead to substantial material wastage, leading to a highly inefficient process, considering the high cost of the feedstock [19].

Additive manufacturing emerges as an appealing option for manufacturing refractory metals and alloys. It offers superior design flexibility, potential for weight reduction through improved design and/or part consolidation, as well as a reduction in lead time, assembly cost, and material waste. Notably, the cost of fabricating refractory materials via AM has been found to be significantly lower compared to machining, even when factoring in additional costs related to powder feedstock (33% more expensive than wrought feedstock), print time, heat treatment, final machining, and waste disposal were included [4].

Consequently, there has been growing interest in AM of refractory metals and alloys. Among the AM techniques, laser powder-bed-fusion (LPBF), laser powder-directed energy deposition (LP-DED), and electron beam powder-bed-fusion (EB-PBF) have been most commonly employed for refractory metals and alloys [20]. Griemsmann et al. [10] examined LPBF of pure Nb with different parameters of laser power, scan speed, and hatch spacing and their effect on part quality. Terrazas et al. [21] performed studies on AM of pure Nb using EB-PBF. C103, an Nb-alloy, is becoming a popular refractory material for AM due to its high weldability compared to other refractory materials such as W and Mo which are more prone to fracture during solidification [19]. AM of C-103 using L-PBF was developed at NASA's Marshall Space Flight Center [4]. Mechanical property testing of the L-PBF demonstrated the ability to achieve properties comparable and in some cases higher than wrought. Philips et al. [1] examined AM of C103 using LPBF and EB-PBF. Process development with C-103 using LP-DED has been successfully demonstrated by NASA [3].

Although AM improves the cost competitiveness for utilizing refractory metals, the deposition technology is not completely matured to consistently produce a material having internal quality and microstructure suitable for critical applications. Because of the inherently high melting temperature of these materials, processing parameters must be closely defined and continually controlled such that the shape of the liquid pool results in a consistent fusion between adjacent melt tracks and layers. The high melting temperatures may impede fusion during deposition if insufficient energy is employed, whereas excessive energy may lead to oxidation or vaporization of other species and defects such as keyhole porosity. The proper selection of energy during processing also has ramifications for the generation of residual stresses, the rate of cooling through the regime that may experience ductile to brittle transition temperature (DBTT), and morphology

and chemical distribution occurring during solidification. In addition, refractory metals have a high affinity for interstitial species, such as oxygen, nitrogen, and hydrogen, and this can lead to the formation of brittle phases and high amounts of porosity and cracking [22]. Hence proper selection of process parameters becomes crucial.

Moreover, defect inspection techniques such as x-ray computer tomography (XCT) and x-ray micro-focus computer tomography (μXCT), which are commonly employed for additively manufactured parts, are unsuitable for the inspection of refractory metal parts due to their high atomic numbers [4]. High atomic numbers result in low penetration of x-rays, leading to low signal-to-noise ratio and unresolved images; let alone defect detection. Refractory material powders being prohibitively expensive, Trial-and-error method to avoid defects is not feasible. Additionally, only a limited number of commercial suppliers offer powder or wire that meets AM specifications. High melting temperatures of refractory metals make powder generation using popular methods, such as inert gas atomization, difficult, further contributing to higher costs [19].

To meet the increased demand from sectors such as aerospace, energy, medicine, and defense, the challenges associated with AM of refractory materials such as cost, defects, and printability need to be addressed. A numerical model simulating the AM process is a powerful tool to mitigate these challenges. It provides a cost-effective alternative to the trial-and-error approach for optimizing the process parameters. In particular, understanding melt-pool evolution, fluid flow, and energy transfer by simulating single or multiple tracks/layers can help obtain optimal process parameters and predict potential defects such as lack of fusion porosity and surface roughness.

1.3 REVIEW OF DED SIMULATION LITERATURE

A variety of numerical models have been developed to model heat transfer and fluid flow during the DED. AM is a complex process involving powder flow, laser energy source, laser-powder interaction, powder-substrate interaction, laser-substrate interaction, melting, solidification, and melt-pool evolution. The evolution of the free surface of the melt pool is modeled by techniques such as arbitrary Lagrangian-Eulerian (ALE), level-set (LS) [23], and volume of fluid (VOF) [24] method. ALE method was employed to model the dynamic shape of the melt pool by Morville et al. [25], Gan et al. [26], Li et al. [27], and Wirth and Wegener [28]. In these works, the powder flow was modeled as Gaussian distribution, without modeling individual particles. ALE can reach high per-degree-of-freedom accuracy near the interface while can be challenging to implement in practice [29]. The LS method is relatively simpler to implement and can more precisely determine the position and curvature of the melt pool free-surface [30]. However, LS is susceptible to mass conservation errors and requires sophisticated measures to be avoided [31]. Nevertheless, some researchers have employed the LS method to model the melt-pool surface evolution, for instance, Han et al. [32], Kong and Kovacevic [33], Qi et al. [34], and Wen and Shin [35].

On the other hand, VOF is strictly mass conservative and has been used extensively in the melt-pool modeling of the DED process. For instance, Lee et al. [36] presented a three-dimensional transport model to study the melt pool formation and melt pool convection flow patterns in Inconel 718 laser deposition. The model considered physical phenomena such as surface tension, laser-powder interaction, fluid motion, mass addition, and solidification. However, the effect of powder addition was modeled in the form of a source term in the equations of conservation of momentum, and energy without explicitly modeling the powder flow. The model predicted the melt-pool geometry and solidification morphology for single-track single-layer deposition and was further extended for multi-layer deposition [37]. Wei et al. [38] developed a multi-track numerical model for predicting the inter-track voids and deposit convexities in laser DED. The model considered the effect of the Marangoni force, mushy zone, Buoyancy force, and surface tension. The model, however, did not incorporate flight dynamics of the powder flow, and the catchment efficiency was determined from the empirical experimental data. Zhang et al. [39] developed a single-track single-layer model for DED of stainless steel to analyze the influence of sulfur concentrations in the substrate on the melt pool dynamics. The model accounted for major physical phenomena such as surface tension, laser powder interaction, mushy zone, Marangoni flow, and laser attenuation due to powder. The laser energy

source was modeled as a uniformly distributed beam and the distribution of blown particles was assumed to be Gaussian. Sun, Guo, and Li [40] developed a numerical model to predict the deposition geometry for high deposition rate DED of stainless steel using ANSYS Fluent. The deposits with single-track multi-layer and multiple-track single-layer were simulated. They assumed powder particles as metal droplets with Gaussian distribution to simplify the model.

All of the above-mentioned VOF-based DED models use analytical techniques to model the dynamics behavior of the powder stream, instead of explicitly modeling the powder particles. While the analytical techniques save the computational cost, they can introduce inaccuracies due to various simplifications imposed [41, 42]. For instance, the powder flow shape is often approximated to be Gaussian, however, it can be different from the idealized Gaussian distribution, depending on the standoff distances and nozzle configurations [42]. Hence, powder feeding with an explicit representation of powder particles needs to be incorporated. However, only a few recent attempts have been made to model powder explicitly with the VOF-based CFD models of DED. For instance, Wang et al. [43] performed single-track multi-layer simulations. Further, this model was employed for Gaussian process regression to predict track geometry. However, the laser source was not explicitly modeled, and the powder source structure was simplified as a quad nozzle arrangement. Bayat et al. [44] developed a model to study the effect of powder flow on dual-track deposition of maraging steel using the commercial software Flow3D. Moreover, the laser-powder interaction was modeled via the ray-tracing method. Both the above models employed the Lagrangian particle model to simulate the powder flow and the VOF method to model the melt pool surface evolution considering major physical phenomena such as the Marangoni effect, surface tension, and Buoyancy forces.

In all the above references, the materials considered are mainly stainless steel, titanium alloys, and other metals with low melting points. There has been only limited work done on refractory alloys such as C103, despite their important applications in aerospace, energy, and defense sectors. The primary challenge in the AM simulation of C103 is the availability of limited data on material properties which makes model validation difficult. There is scarcity of thermophysical properties in the literature for C103. Sparse data exist for these thermophysical properties at room temperature, while good temperature-dependent data is virtually non-existent within the open literature. Recently, Dalagan [45] simulated the melt pool formation of C103 using ANSYS Fluent. However, the powder flow, surface evolution, and the formation of deposit based on surface-tracking were not modeled. Moreover, the model was not validated with experiments. The thermophysical properties of C103 were computed based on the properties of the constituent elements. However, these can be different from the properties of the alloy and can lead to inaccurate model predictions.

Moreover, most works on DED simulation, which model melt-pool evolution and powder flow, consider single/dual-track and single/dual-layer printing to reduce computational efforts. These simulations can to a certain extent provide insights on powder spreading and deposit formation in early stage of DED, while they are still far from the real process, and do not provide information on how the continuous tracks and layers interact with each other in the printing process. In other words, it is necessary to perform systematic and comprehensive numerical investigations on the printing of multiple layers with multiple tracks in DED process.

1.4 PROPOSED APPROACH

In this report, a multiphase, multi-physics simulation has been developed for blown-powder DED of C103. The material properties of C103 are obtained from existing literature and thermodynamic simulation tool, ThermoCalc. The VOF-Lagrangian model in Star-CCM+ now incorporates powder impingement, melt pool formation and evolution, as well as sonification. It also considers the effect of machine zone, surface tension, and its gradient on the quality of build. The developed model is validated with single bead experiments and extended to multi-tracks, and multi-layers to investigate the effect of power, scan speed, hatch spacing on both defects and part dimensional quality, e.g., lack of fusion, inter-track voids, and

surface roughness. Finally, various process maps were established to guide CCAM in building a practical part with minimal defects and desired part quality.

2. TECHNICAL RESULTS AND DISCUSSION

2.1 EXPERIMENTATION OF POWDER DIRECT ENERGY DEPOSITION

2.1.1 Material Deposition: SS316L and C103

CCAM and ORNL team used its expertise in building parts with SS316L and C103 part using powder DED. Four depositions were made on each single bead at different power and speed settings in Table 1. Three laser powers of 600W,800W, and 1000W, and two speeds of 500 mm/s and 700 mm/s were selected for the SS316L trial builds. The measured width of deposit was increased from 1.48 mm to 1.87 mm with an increase in laser power, while the increase in height is negligible, by 0.02 mm. The laser spot size and powder mass flow rate were 1.38 mm and 0.27 g/s, respectively. The deposits of SS316L were used to verify the correctness of physical interactions developed in the simulation. Additionally, two cases of C103 were deposited on different substrate materials of C103 and Ti by ORNL and CCAM. Double-bead with single layer in Table 2 was deposited at ORNL on C103 substrate to verify the obtained material properties from literature and thermodynamic calculation. Thirty-eight samples were created at CCAM in various power, scan speed, powder mass flow rate, and working distance in Table 3 to validate the model and construct process map for CCAM.

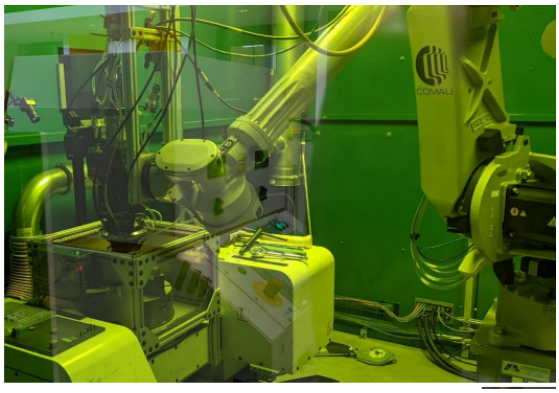

Figure 1: Powder direct energy deposition system at CCAM

Table 1. Process parameters used for 316L validation trials.

# Sample	Power	Scan speed	Measured Width	Measured Height
Units	W	mm/min	mm	mm
1	600	500	1.48	1.22
2	800	500	1.76	1.24
3	1000	500	1.87	1.24
4	800	700	1.50	1.00

Table 2. Process parameters used for C103 double-bead deposit on C103 substrate.

# Sample	Power	Scan speed	Powder mass flow rate	Stepover	Nozzle Offset

Units	W	mm/min	g/s	mm	mm
1	466	1300	0.063	0.333	3.5

Table 3. Process parameters used for C103 single-bead deposit on Ti substrate.

# Sample	Power (P)	Scan speed	Powder mass flow rate	Layer increments	Nozzle offset
Units	W	mm/min	g/s	mm	mm
1	650	500	0.294	0.5	156
2,	850	500			
3	1050	500			
4	650	350			
5	850	350			
6	1050	350			
7	650	650			
8	850	650			
9	1050	650			
10	650	350			
11	850	500	0.217		
12	1050	650	0.294		
1	650	350	0.294		
	850	500	0.217		
	1050	650	0.294		
25	850	500	0.370	0.325	155
26			0.294		156
27					157
28					158
29	850	500			159
30					160
31					161
32					162
33					163
34					164
35					165
36					166
37					161
38				0.5	161

2.1.2 Defects and Microstructure Analysis

Metallographic analyses were carried out for the printed C103 specimens using optical microscopy (OM) and electron backscatter diffraction (EBSD) to investigate the influence of process conditions on defect formation and microstructural change. The thirty-eight parts given by CCAM were sectioned parallel to the build direction. The sectioned samples were polished using abrasive grit papers and finished with 0.05 μm colloidal silica. The remaining surface imperfections are removed using Hitachi ArBlade 5000 ion milling machine at 6 kV. The OM was conducted in a Zeiss Axio Imager, and the images were captured using Zeiss ZEN Core 3.5 software. The images were post-analyzed using ImageJ (NIH, Maryland, USA) to identify defects. The OM images are taken from the top, middle, and bottom regions for each sample, depending on it height. The optical micrographs of the thirty-eight samples are provided in Appendix 7. The grain morphology and other microstructural features were analyzed using EBSD, a Zeiss Gemini SEM 450 equipped with a backscattering detector (Bruker, Billerica, MA, USA), for three samples 7, 8, and 9 in Table 3.

2.2 APPLICATION OF PHYSICAL INTERACTIONS TO MELT POOL SIMULATION

In this section, the development of computational fluid dynamics (CFD) melt pool simulation is described in terms of physical interactions among the heat source, material, and manufacturing parameters. Preliminary simulation trials were conducted using 24–48 cores of ORNL's Libby machine maintained by Nuclear Energy Fuel Cycle Division (NEFCD) to develop the CFD modeling framework, verify the setup, and validate the physics associated with DED. Further simulations typically used 64–128 cores on ORNL's RIDGE and LILLY high-performance computing (HPC) systems maintained by Compute and Data Environment Science (CADES) and NEFCD.

2.2.1 Modeling governing equations

Modeling of DED process typically involves multiphase flow with three phases: a solid phase for substrate, gas phase for the shielding gas, and solid particles for the powder in Figure 2. The particles injected from the nozzle create powder cloud and interact with laser heat source and Ar-gas during flight. Then, the heated particles from the laser impinge on the substrate and form a deposit. The portion of the particles colliding the melt pool on the substrate only contributes to form the deposit while the rest are bounced off. The flow in the melt pool is assumed to be incompressible Newtonian flow. Volume of fluid (VOF) method is used for modeling gas-substrate phase and tracking the evolution of free surface at the melt pool surface. The particles entering toward the melt pool are modeled using the Lagrangian particles method and tracked using kinematic equation based on Newton's second law of motion. All particles are assumed to be spherical, and identical thermo-physical properties of substrate are used for particles.

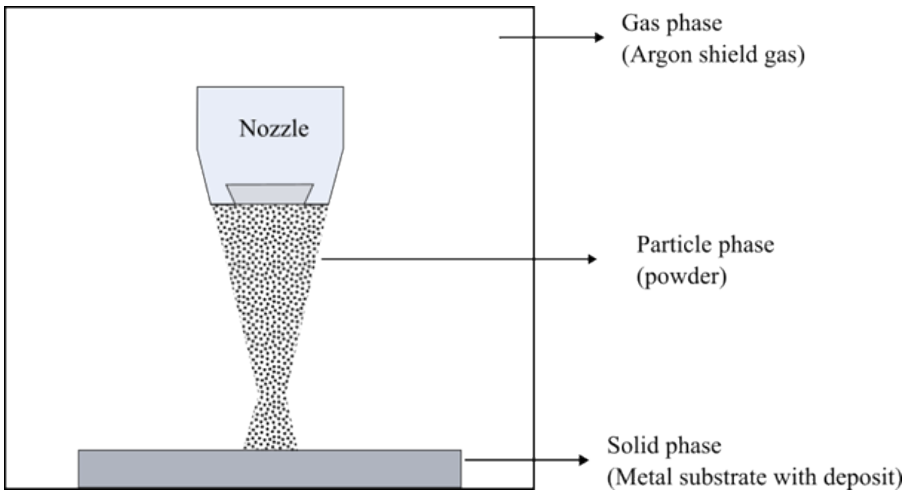

Figure 2: Different phases involved in a DED process

The simulation was developed based on Star-CCM+, a commercial CFD software. The model numerically solved the conservation equations of mass, momentum, energy, and fluid volume fraction, which are as follows:

Mass:
$$\frac{\partial \rho}{\partial t} + \nabla.(\rho \boldsymbol{V}) = S_M \quad (1)$$

Momentum:
$$\frac{\partial \rho \boldsymbol{V}}{\partial t} + \nabla.(\rho \boldsymbol{V}\boldsymbol{V}) = -\nabla p + \nabla \mu(\nabla \boldsymbol{V} + \nabla \boldsymbol{V}^T) + M_p + M_{mushy} \quad (2)$$

Energy:
$$\frac{\partial \rho H}{\partial t} + \nabla.(\rho \boldsymbol{V} H) = -\nabla.(k \nabla T) + q_p + q_{Laser} + q_{fusion} \quad (3)$$

Volume of Fluid:
$$\frac{\partial \alpha}{\partial t} + \nabla.(\boldsymbol{V}\alpha) = F_p \quad (4)$$

where ρ is the volume-averaged density, $\boldsymbol{V}$ is the mixture velocity**,** p is the pressure, S_M and M_p are respectively the mass and momentum transferred from particle to solid phase. M_{mushy} is damping term at mushy melt zone region modeled as porous region. In the energy conservation equation, H is the mixture enthalpy, and T is the mixture temperature and k is the volume-averaged thermal conductivity of the mixture. q_p is the heat transfer from particle to substrate or phase change heat transfer, q_{Laser} is the heat source due to laser, q_{fusion} is the heat of fusion. Finally, in the VOF equation, α denotes the volume fraction of the solid phase with value between 0 and 1 while F_p is the volume fraction source due to particle entrance into the solid phase. The volume-averaged quantities are computed using α, for instance, $\rho = \alpha \rho_{sub} + (1-\alpha)\rho_{gas}$ where ρ_{sub} and ρ_{gas} $are\ the$ densities of solid and gas phases respectively.

2.2.2 Incorporation of physical interactions into model

2.2.2.1 Interaction between laser and substrate

The energy of laser beam is absorbed by the substrate surface, resulting in heat production at the interface and subsequent melting of the substrate. This heat source can be modelled as a surface source (W/m^2), however the area required to calculate the heat source on the substrate-gas interface for each timestep is non-trivial due to the diffusion of the interface in Star-CCM+. Therefore, the surface heat source should be converted to a volumetric heat source to avoid problems associated with numeric. For this purpose, a Continuous Surface Force (CSF) model treatment is used to transform surface heat source into volumetric heat source [40] as shown in Eqn. 5 and illustrated in **Error! Reference source not found.**.

$$q_{Laser} = \eta_L Q_l \, |\nabla \alpha| \frac{2\rho_{surf} c_{psurf}}{\rho_{sub} c_{psub} + \rho_{gas} c_{pgas}} \quad (5)$$

$$Q_l = \frac{2P}{\pi r_{beam}^2} \exp\left(\frac{-2r^2}{r_{beam}^2}\right) \quad (6)$$

In Equation (5), the term $\frac{2\rho_{surf} c_{psurf}}{\rho_{sub} c_{psub} + \rho_g c_{pg}}$ plays a role in redistributing the heat source over the liquid phase at the gas-liquid interface. Here, $\rho_{surf} = \alpha\rho_{sub} + (1-\alpha)\rho_{gas}$, $c_{psurf} = \frac{\alpha\rho_{sub} c_{psub} + (1-\alpha)\rho_{gas} c_{pgas}}{\rho_{surf}}$. The term $|\nabla \alpha|$ represents the gradient of volume fraction and incorporates the of the CSF method to define the laser as a volumetric surface heat source. η_L is the absorption coefficient, which is a constant. In Equation (6), P is peak power, r_{beam} is the radius of the laser spot, and r is the radial distance of a point from the center of the laser beam.

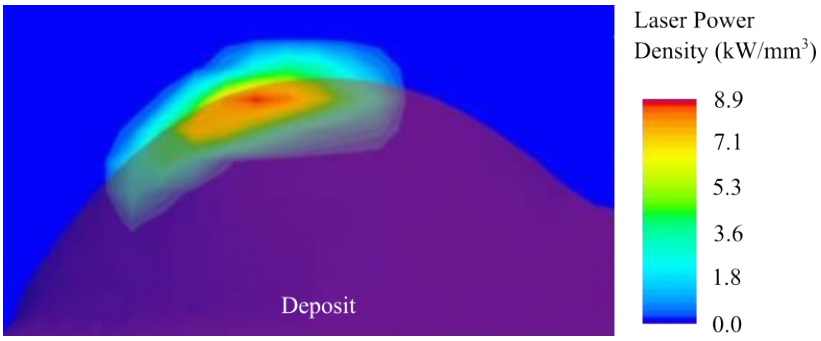

Figure 3: Volumetric Laser Energy source profile

The absorptance of laser beam used to form the deposit on substrate is a key process parameter. Approximately half of the incident beam is reflected by the substrate, 10% of the energy is lost through the powder cloud, and an additional 1% is lost by air convection and radiation. The absorptance of laser beam was determined based on the values from DED literature for stainless steel alloy [39, 40, 46, 47], which falls in the range of 30%~50%. Thus, the absorptance of 40% selected in this work is considered reasonable. The gaussian shape was assumed for the laser beam distribution on the substrate [40]. A semi-implicit treatment of surface tension force was applied in the model using High Resolution Interface Capturing Scheme (HRIC) with sharpening factor of 0.2. The semi-implicit treatment ensures smooth evolution of the substrate-gas interface leading to an error-free volumetric heat source distribution at the interface in Star-CCM+.

2.2.2.2 Modeling of liquid to solid phase transformation

The deposit in DED undergoes phase transformation from liquid phase to solid phase. However, the VOF method in Star-CCM+ does not explicitly account for the liquid to solid phase transformation. Instead, it defines the fraction of fluid in a simulation cell based on the estimated values from non-dimensional temperature defined in Eqn. 7. For instance, if the value of non-dimensional temperature T^* is greater than 1, the cell is treated as liquid. If the value is less than 0, it is treated as solid in Eqn. 8.

$$T^* = \frac{T - T_{solidus}}{T_{liquidus} - T_{solidus}} \quad (7)$$

$$\alpha_{liq}^{*} = \begin{cases} 0\ (solid) & when\ T^{*} < 0 \\ T^{*} & when\ 0 < T^{*} < 1 \\ 1\ (liquid) & when\ 1 < T^{*} \end{cases} \quad (8)$$

where α_{liq}^{*} is the fraction of liquid present in the metallic (solid) phase, $T_{solidus}$ and $T_{liquidus}$ are the solidus and liquidus temperatures of the material respectively.

In Star-CCM+, the phase changes are considered only in the enthalpy equation and the momentum equation does not account for the fluid flow in the melt pool region and the mushy zone. A combination of Carmen-kozeny and Metzner model is additionally incorporated into the model to accurately represent fluid flow in the molten pool region [39, 40]. These models are active throughout the entire computational domain, detecting the melted region using Eqn. 8 to assign liquid metal viscosity and applying the forcing term proposed by Carmen-kozeny (M_{mushy}) to the momentum equation (Eqn. 2) to account for fluid flow in mushy zone with solid fraction > 0.3. The VOF model considers the solid metal substrate as a liquid with finite viscosity, therefore the flow in the solid region does not come to a full stop, as expected for rigid solids, this creeping flow causes the interface to spread over time resulting in erroneous prediction of the width and height of the melt pool. The flow in the computational cells within the solidified region is enforced to 0, when the solid fraction reaches 0.8 or higher, by the flow stop model within Star-CCM+ and enforces pressure inside the cell to a reference pressure, which is typically the atmospheric pressure.

2.2.2.3 Variation of surface tension

The gradient of surface temperature across the melt pool region causes fluid convection due to the surface tension force and its gradient. Such Marangoni flows have significant impact on fluid convection in the melt pool and the geometrical shape of melt pool and deposit. The surface tension force at the solid-gas interface should be zero. However, with the default setting of Star-CCM+, since the solid region is modeled as liquid with large viscosity, the surface tension acted even at the solid-gas interface and consequently led to unrealistic motion of melt pool in the solidified region in Figure 4. To resolve this unrealistic issue, the surface tension force is set to be zero for solid fractions greater than 0.9 in Figure 5, which stops the interface motion as it approaches to solid fraction 1.

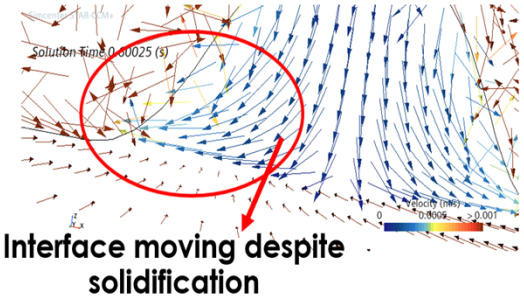

Figure 4: Velocity vectors on a cross-section of the solidified 316L alloy

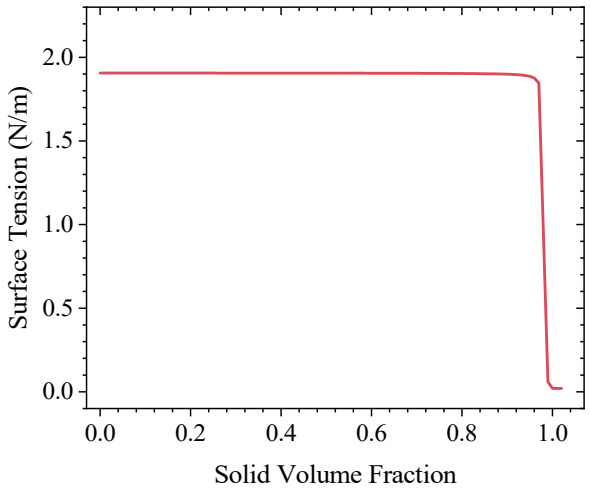

Figure 5: Surface tension coefficient vs. solid fraction.

In addition, a simulation study was conducted using a 'flow stop' model available within Star-CCM+ to address unphysical inward stretching of solid-gas interface, as marked in red in Figure 6. Further investigation in Figure 7 was conducted to isolate this unphysical behavior. It was revealed that there is a development of negative pressure in the proximity of the interface, which drives the interface in an inward direction.

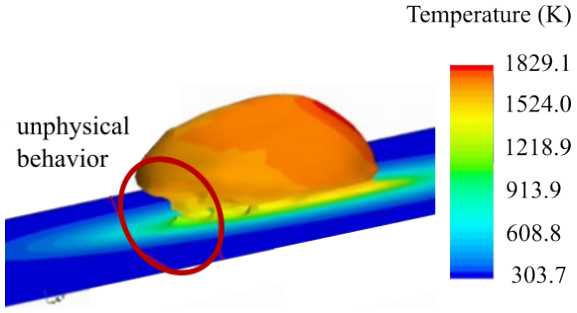

Figure 6: Evolution of melt pool shape with the addition of 'flow stop' feature within StarCCM+.

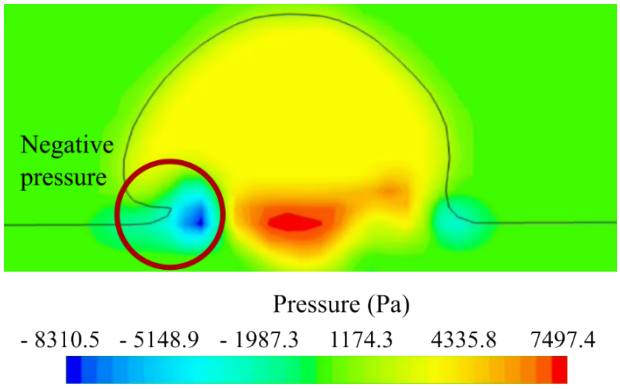

Figure 7: Pressure distribution on a cross-section of the melt pool in the direction of the scanner.

The variation of surface tension over the melt pool region causes the molten metal to flow from lower surface tension to higher surface tension region. This phenomenon is called Marangoni flow. This flow changes fluid convection pattern in the melt pool and consequently affects the melt pool and deposit shape.

Figure 8 shows two predicted deposit topologies (a) with and (b) without considering Marangoni flow. Irregular deposit morphology with ragged edges is observed for the simulation with Marangoni convection in Figure 8(a), while smooth morphology was found without Marangoni in Figure 8(b). The effect of Marangoni convection on the deposit geometry seems to be negligible compared to the printed deposit in Figure 8(c), which is relatively smooth. Therefore, Marangoni convection is ignored in the current study to improve computational efficiency.

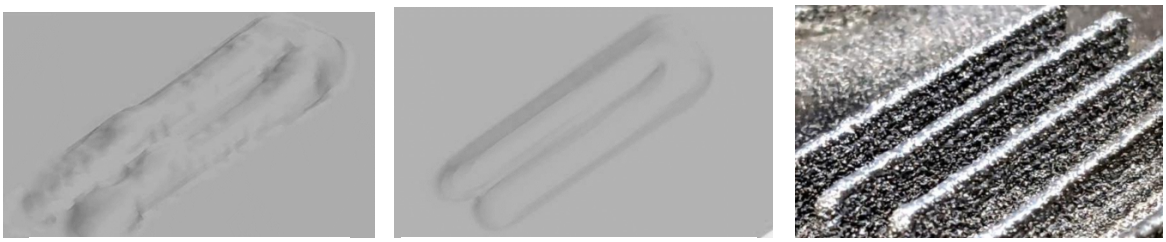

(a) With Marangoni effect (b) Without Marangoni effect (c) Experiment

Figure 8: Effect of Marangoni convection on deposit topology: (a) with Marangoni, (b) without Marangoni, and (c) deposited build. The effect of Marangoni flow on build geometry is minimal so it is neglected in the simulation to obtain computational efficiency.

2.2.2.4 Modeling motion of the spray nozzle:

In the DED process, the powder particles are blown from the nozzle so the motion of the nozzle (i.e., velocity and path) controls the shape of the melted deposit. The motion of nozzle is explicitly modeled using the overset mesh method, where the *nozzle mesh* in Figure 9 travels through a static *background mesh*, which contains the substrate. The flow solution in the *nozzle mesh* is coupled to the *background mesh* by interpolation and solution mapping in Star-CCM+.

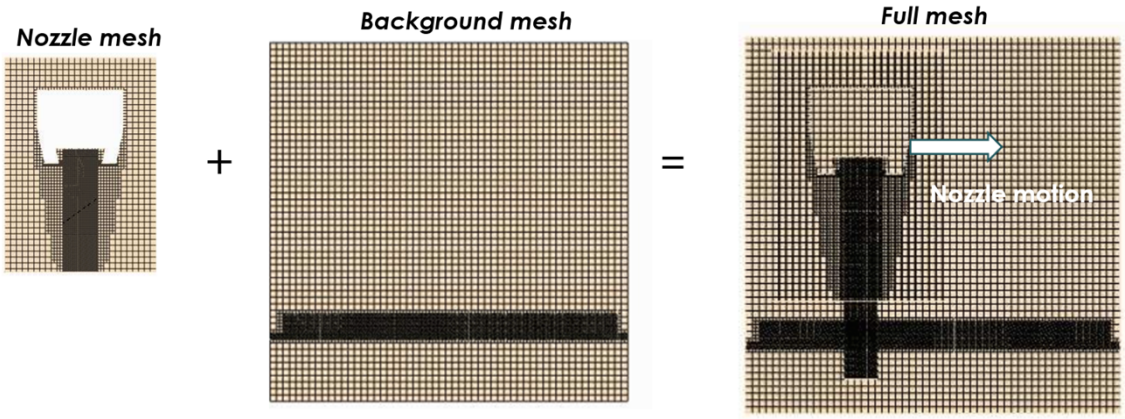

Figure 9: Modeling of nozzle motion in Star-CCM+, overset mesh method was used to account for nozzle motion in which nozzle mesh is combined with background mesh for solution.

The nozzle translates on XY plane and in z-direction with different velocity components (*Vx Vy, Vz)*. Although various x-, y-, z-velocity can be set in the model, the builds in section 2.1 were deposited using bi-directional tool path so only bi-directional tool path was investigated in this work. There can be acceleration or deceleration in the nozzle velocity while skywriting, but it may cause excessive

computational costs. Therefore, a constant nozzle velocity was used for single and multi-track/multi-layer simulation in later sections, except for transitions in direction. The transient changes in nozzle velocity profile are shown in Figure 10.

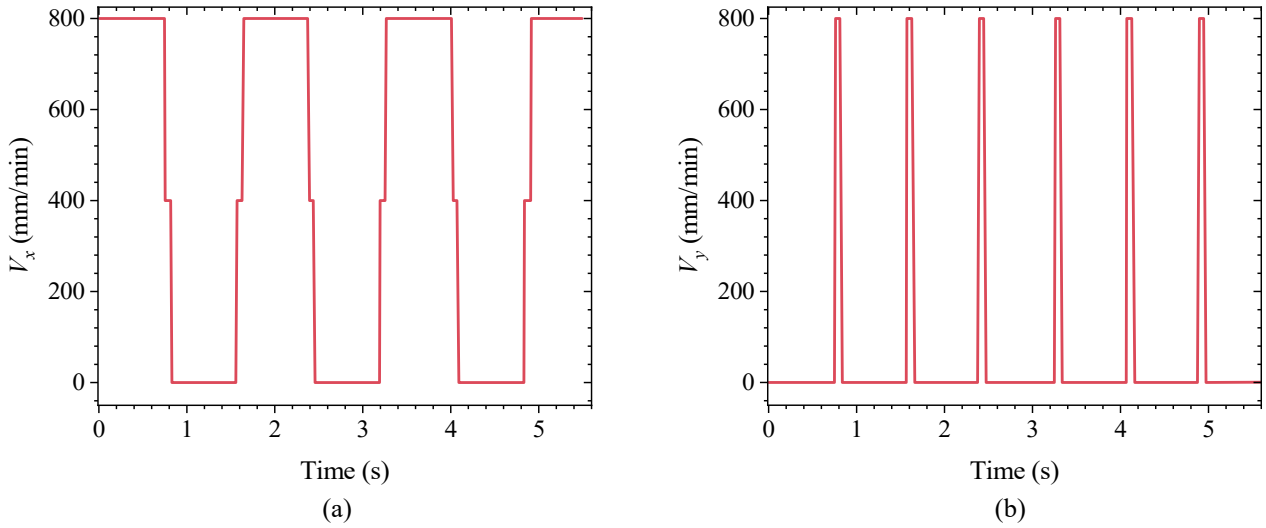

Figure 10: Profile of nozzle motion over time, (a) velocity in x-direction, *Vx*, and (b) velocity in y-direction, *Vy*

2.2.2.5 Modeling of powder particles:

The motion of particles injected from the nozzle is modeled using a Lagrangian particle tracking approach using the kinematic equation given in Eqn. 9. The two significant inter-phase forces governing the particle motion are the drag force and the pressure gradient force. A drag law with Schiller Naumann drag correlation traditionally used for gas-particle flows is adopted to account for the drag force (F_d) and the pressure gradient force (F_d) is computed based on the gradient of the spatially varying pressure field of the continuous fluid around the particles. Mass (M) of the particle is estimated based on the particle size defined at the inlet and the density of the particle, which is typically the density of the solidified deposit. The particles are assumed to be spherical and of constant size, which is prescribed at the inlet of the injector. The particle temperature evolution is computed using Eqn. 10. The heat loss due to radiation is assumed to be small [36] and hence neglected in Eqn. 10. The heat exchange between the background gas flow and the particles are estimated using Newton's law of cooling in Eqn. 11, where the heat transfer coefficient is calculated using well established Ranz Marshall correlation for gas particle flows. Other inter-phase forces such as buoyancy, lift and virtual mass force, which are only significant for gas-liquid flows are assumed to be negligible and not considered in Eqn. 9.

$$m_p(\mathrm{dv_p})/\mathrm{dt} = F_p + F_d + m_p g \tag{9}$$

$$m_p c_p \frac{dT_p}{dt} = q_b \tag{10}$$

$$q_b = h\left(T_p - T_g\right)\pi d_p^2 \tag{11}$$

where m_p is the particle mass, $\boldsymbol{v_p}$ is the particle velocity, $\boldsymbol{F_d}$ is the drag force, $\boldsymbol{F_p}$ is the Pressure gradient, M is the mass of the particle, T_p is the particle temperature, T_g is the temperature of the gas, d_p is the particle diameter, and h is the heat transfer coefficient.

2.2.2.6 Transferring particles into melt pool/deposit interface:

A VOF-Lagrangian impingement model in StarCCM+ is used to account for the particle transfer to the melt pool region. In the model, actual mass transfer from particles to the substrate occurs only when the particles enter the melt pool/deposit interface, where the computational cell at the interface in Figure 11 has a volume fraction of 0.0001< VOF <0.5 and a temperature equal to or above the liquidus temperature of the material. When the particles are transferred to the melt pool, their mass, momentum, and energy are also transferred. If the particles do not meet these VOF and temperature conditions, the particles are removed from the computational domain using the parcel depletion criteria.

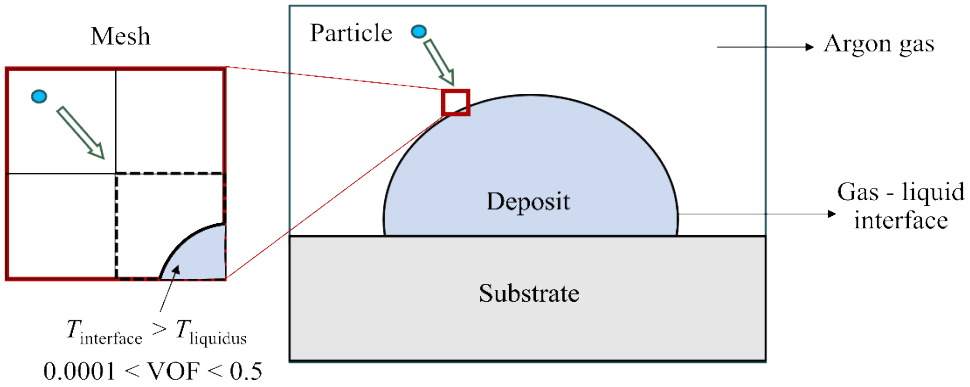

Figure 11: Boundary criteria of VOF and temperature for particle transfer from nozzle to melt pool and/or deposit. Particles only contribute to form the deposit when VOF values are in between 0.0001 and 0.5 and a temperature is equal to liquidus of the material or above.

2.2.2.7 Obtaining of material properties of C103

The temperature dependent thermo-physical properties are necessary to run the melt pool model. However, the property database of refractory C103 is not well-established and scarcely reported in literature. The material properties were calculated on the assumption of mixing of properties from the key alloys: 88.3% Nb; 10% Hf; 1% Ti; 0.07% Zr [45]. The properties of density, specific heat, and thermal conductivity were calculated on the law of mixture. Viscosity and surface tension coefficient were assumed of Niobium. The other properties of solidus, liquidus and heat of fusion were calculated with the composition above using thermodynamic tool, ThermoCalc. The properties are summarized in Table 4. The temperature dependent properties of specific heat and thermal conductivity of C103 are plotted in Figure 12. It is assumed that thermal conductivity and specific heat attains a constant value when the metal reaches the liquidus temperature and remains a constant above the liquidus temperature.

Table 4 Thermo-physical properties of C103 used in the simulation [45]

Properties	**Temperature (K) range**	**Equation/value**
Density (kg/m3)	8265	Composition based (88.3% Nb; 10% Hf; 1% Ti; 0.07%Zr)
Specific heat (J/kg-K)	$T < 543$	$c_p = 196.27 + 0.249T$
	$543 \leq T < 2747$	$c_p = 0.0705T + 222.87$
	$T \geq 2747$	$c_p = 434.96$
Thermal conductivity (W/m-K)	$T < 2677$	$k = 0.0125T + 24$
	$T \geq 2677$	$k = 57.46$

Viscosity (kg/m-s)	constant	0.0052 (Nb)
Heat of fusion (J/kg)	constant	204338 [Thermo-Calc]
Solidus Temperature (K)	constant	2277 [Thermo-Calc]
Liquidus Temperature (K)	constant	2680 [Thermo-Calc]
Surface tension coefficient (N/m)	constant	1.937 (Nb)

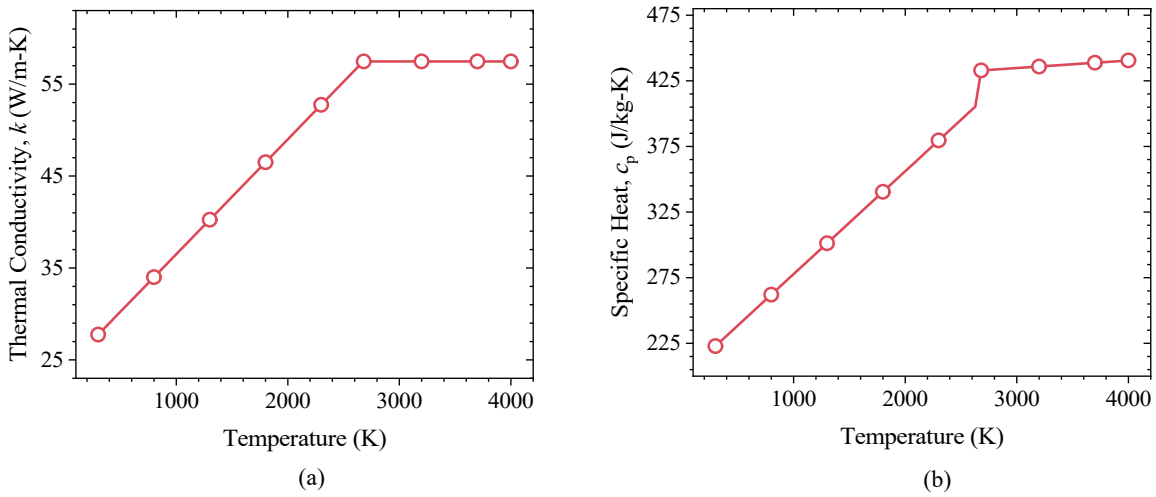

Figure 12: Temperature dependent thermal conductivity and specific heat of C103 used for the simulations: (a) thermal conductivity and (b) specific heat.

2.3 Tool path: Skywriting

Skywriting is a tool path strategy used in the metal AM to minimize overheating at the turn, defect formation, and material waste. The nozzle moves to the starting point of the track to start the second track, in contrary to the continuous raster patten. A two-track deposit of C103 was performed using skywriting strategy in Figure 13. An attempt was made to run more than two tracks with skywriting, however, the predictions for more than two tracks resulted in unphysical morphologies, therefore, all the multi-track/multi-layer simulations in the report are with continuous printing without skywriting. Figure 14 shows the cross-section on YZ plane. A slightly taller deposit was observed at the second track.

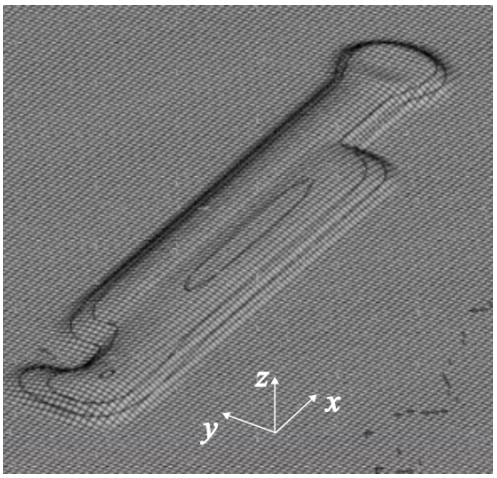

Figure 13: A two-track simulation with skywriting

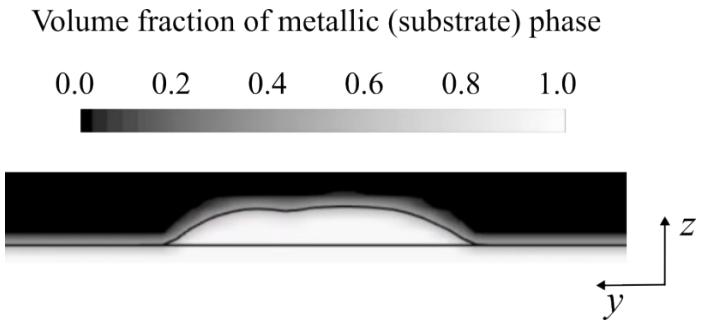

Figure 14: Cross-section of the deposit with skywriting

2.4 MODEL VALIDATION

2.4.1 Validation of multi-physics interactions using SS316L build

A validation study of the multi-physics framework developed using SS316L is conducted, as the material properties of SS316L are well-established and widely reported in the literature. Therefore, rigorous validation of the physical interactions corrected in the Star-CCM+ simulation is feasible. The process parameters used for the validation study were given in Table 1. Figure 15 and 16 show the variation of deposit (a) width and (b) height with increase of power and scan speed, respectively. The trend of the predicted geometry is analogous to the measured deposit geometry. In Figure 15, it can be observed that the deposit width and height increase with an increase in power, while in Figure 16, both the width and height decrease with a decrease in the scan speed. It can be concluded that the heights of the melt pool deposits predicted by the simulations for various powers and scan speeds compares reasonably well with the experimental values, however, a discrepancy in the solidified pool width dimension was identified compared to the experiment. As discussed in 2.2.2.3, the unphysical stretching motion on the interface of the solidified region, caused by surface tension force, led to the discrepancy between the prediction and measured width. Subsequently, the models are calibrated and corrected for surface tension coefficient, overset mesh, and flow-stop to enhance prediction quality. The calibrated model was then used for validation with C103 material in the following subsection.

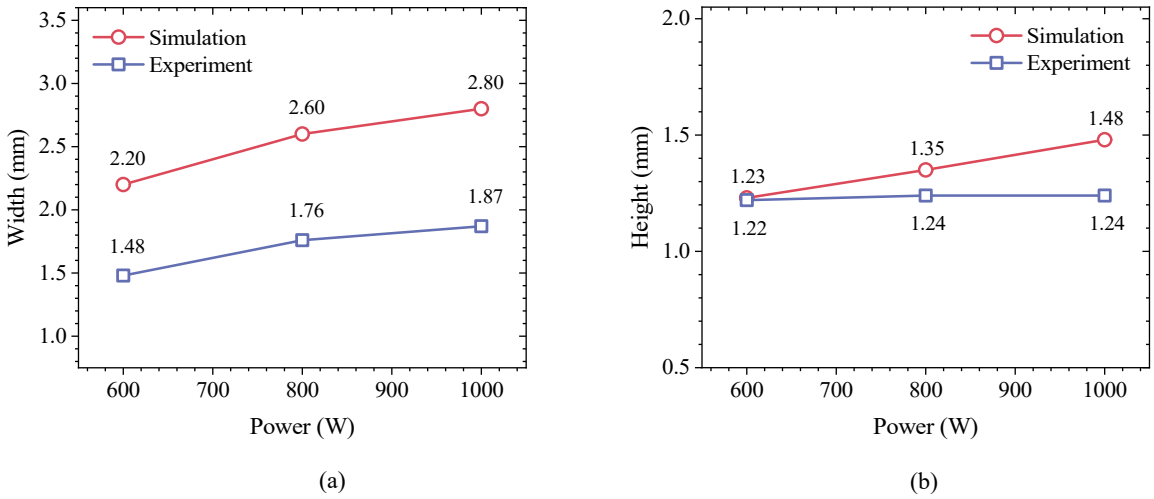

Figure 15: Deposit (a) width and (b) height compared to experiment for different laser powers.

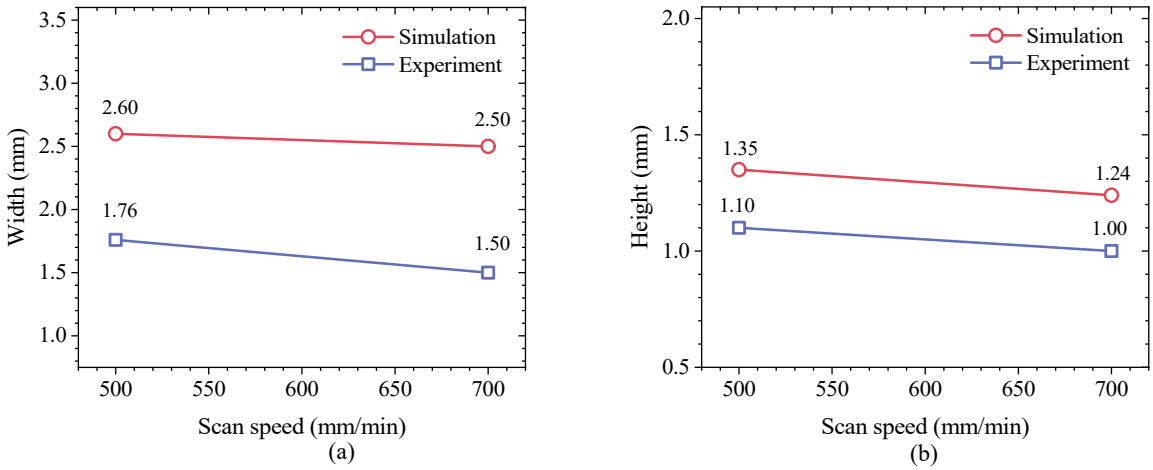

Figure 16: Deposit (a) width and (b) height compared to experiment for different scan rates.

2.4.2 Model validation with refractory material C103

Figure 17 shows single track C103 deposits at three laser powers of 650W, 850W, and 1050W with a constant speed of 500 mm/min. The widths of the deposits progressively increase with power. It indicates that the width of the deposit is primarily determined by the power, with higher laser power resulting in a wider deposit width. Furthermore, quantitative measurements of the width and height of the deposits for different powers were conducted based on the simulation results and compared them to the measured values in Figure 18. The trend for the variation in width and height is consistent with the measured values. The deposit width increases from 1.2 mm to 1.6 mm by 33% in prediction and from 1.4 mm to 1.9 mm by 35% in measurement, whereas the height increases from 0.41 mm to 0.45 mm by 9.7% in prediction and from 0.31 mm to 0.37 mm by 19% in measurement. The height increases by approximately 0.06 mm in measurement, whereas the width increases by 0.5 mm, showing a significant difference in magnitude. It indicates that the power primarily determines the width of the C103 deposit and less influence on the height. Note that in these validation trials, the powder mass flow rate had to be adjusted to account for the catchment efficiency to match the heights of the deposits with the experimental values.

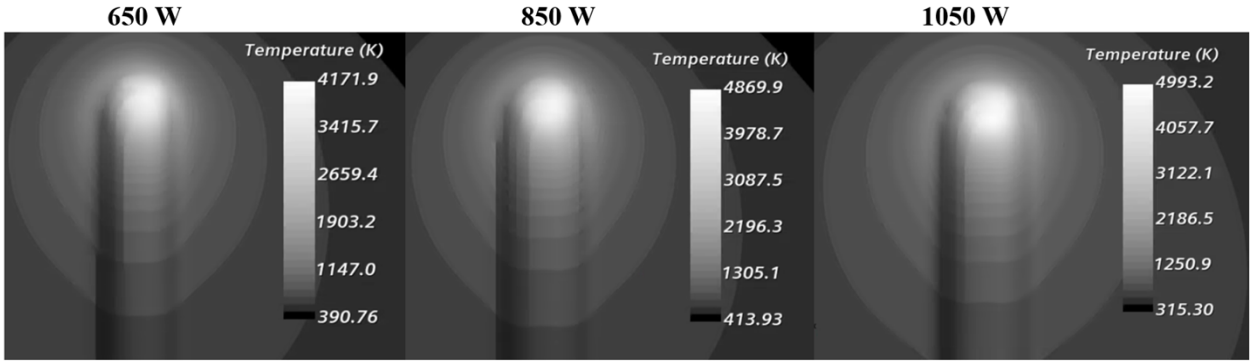

Figure 17: Top view of deposits of C103 for three laser powers for a fixed scan speed of 500 mm/min

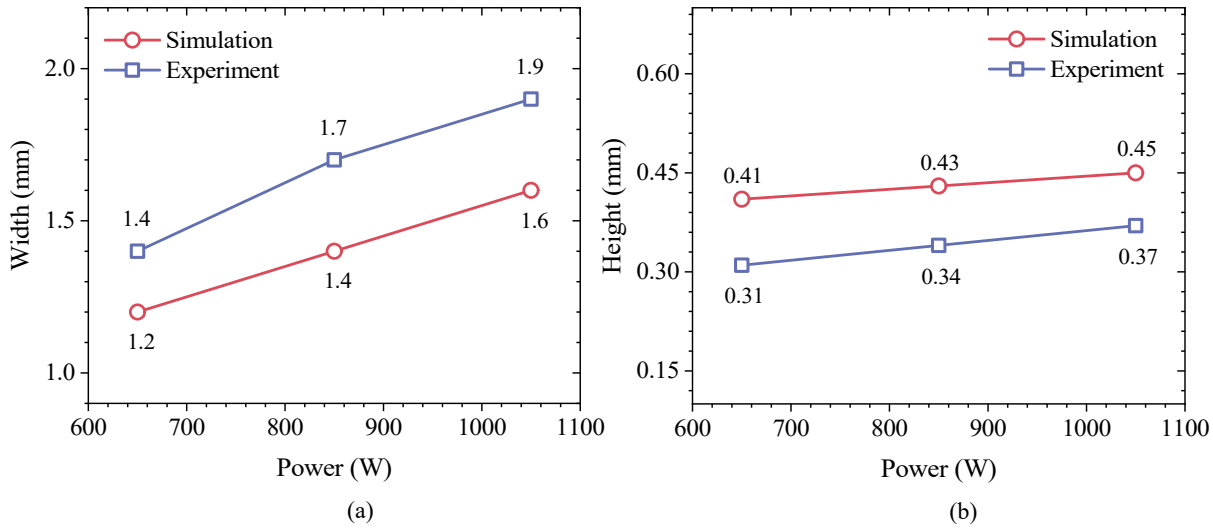

Figure 18: Deposit (a) width and (b) height predicted by simulation compared with experiment for scan speed 500 mm/min.

Figure 19 shows YZ cross-sections from first track and double-track deposit with a single layer printed at ORNL. The experiment was conducted on C103 substrate, while the CCAM build was printed on Ti substrate. The measured width and height of the deposit from a single track are 663 µm and 212 µm in Figure 19(a). The width and height of the double-track are 1090 µm and 218 µm. The deposit width is increased by 64% as the second track deposits. However, the height increase is insignificant, increased only by approximately 3%.

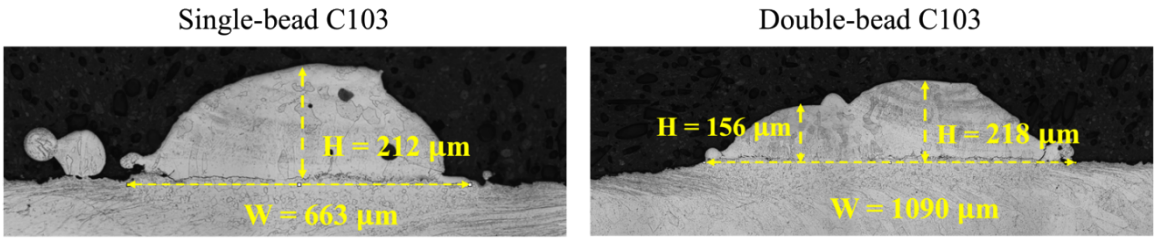

Figure 19: YZ cross-section of C103 deposit.

Figure 20 shows a comparison of the predicted to the measured width and height. Overall, the predicted width and height are fairly consistent with the measured ones. The predicted height and width are 207 µm and 800 µm for the single-track and 244 µm and 1200 µm for the double-track. The deviation of prediction is 3% for single-track and 12% for double-track in height and 20% for single-track and 10% for double-track in width. For all practical purposes, the deviation error in the model is acceptable and therefore, it is used in the subsequent sections to study the fusion characteristics of C103.

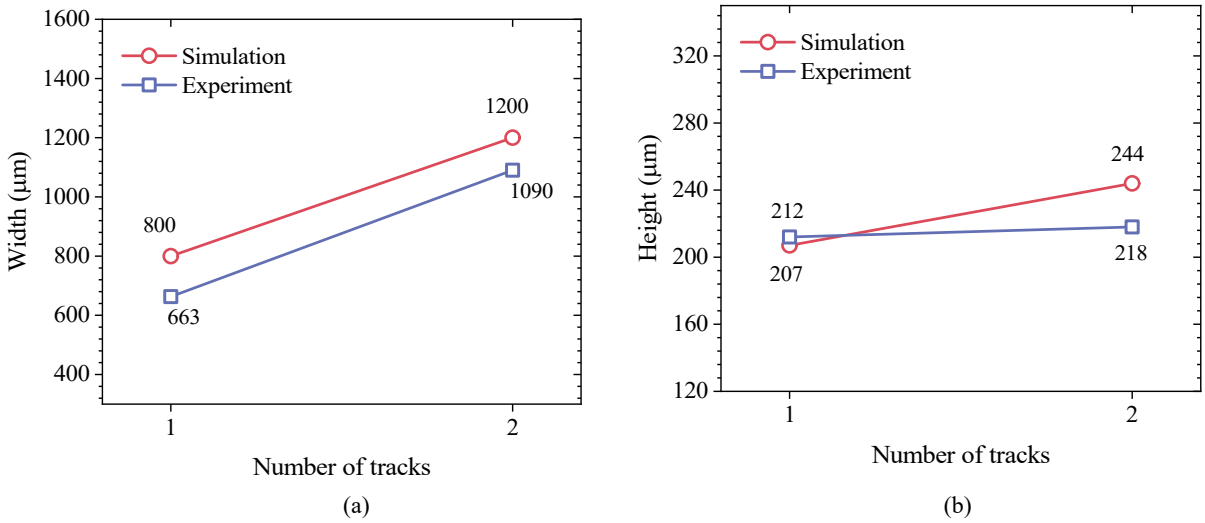

Figure 20: Deposit (a) width and (b) height predicted by simulation compared with experiment for single track and double tracks.

2.5 INFLUENCE OF PROCESS PARAMETERS ON DEPOSITION QUALITY OF C103

The validated simulation was used to investigate the effect of key process parameters on deposit geometry: 1) scan speed, 2) laser power, and 3) hatch spacing. A single layer deposit with eight-tracks in Figure 21 was simulated with the three conditions of each process parameter. The fusion characteristics of the deposit were assessed from XY cross-section plane on three monitoring locations along plane 1, 2 and 3 marked in red dashed line in Figure 21. Also, the height of the deposit is estimated by averaging the minimum and maximum height of each track on the deposit. The representation of the height profiles from the locations is shown in Figure 22.

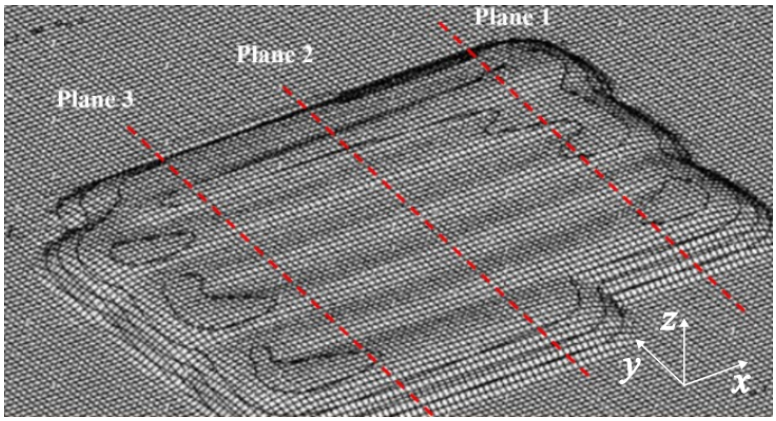

Figure 21: A representation of different planes considered for fusion assessment study.

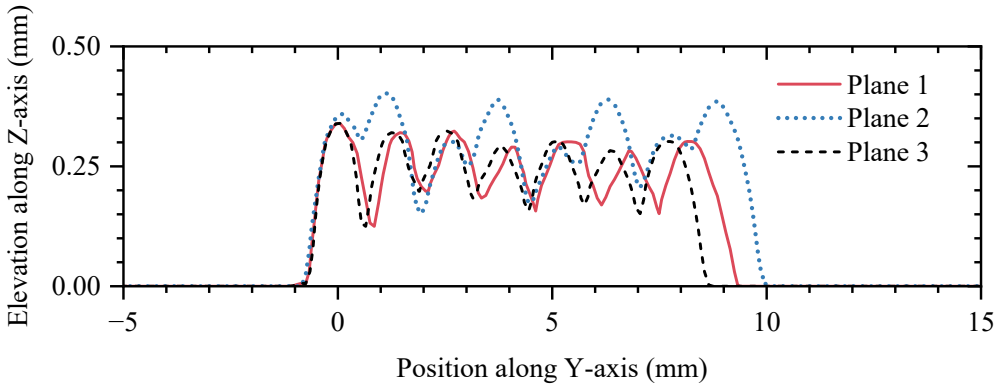

Figure 22: A representation of the elevation of the deposit-air interface curves on three planes to estimate the height of the deposit.

2.5.1 Deposition of multi-track on single layer: Effect of scan speed

Effect of three scan speeds: 350 mm/min, 650 mm/min and 800 mm/min, on the fusion characteristics and deposit height of C103 were assessed at a constant power of 1250 W. The cross-sectional view of the deposits on all the sample planes considered for each scan speed are provided in Figure 23. It can be observed that the fusion between adjacent tracks is reasonably good for all scan speeds for the laser power of 1250 W. The height of the deposit decreases with increase in scan speed. When the scan speed is slow, the beam residence time becomes longer, resulting in a higher mass injection per unit length leading to taller deposits compared to the deposits generated with faster scan speed. The value of the heights of the deposit for different scan speeds is provided in Figure 24. It appears that for slower scan speeds than 650 mm/min the height of the deposit reduces significantly with increase in scan speed and for scan speeds above 650 mm/min the deposit height reduces gradually, almost nearing a constant value.

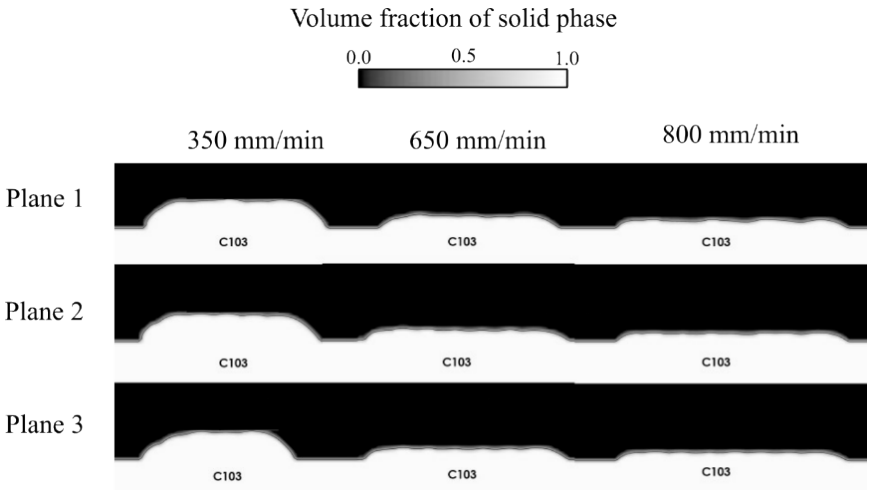

Figure 23: Deposit geometry predicted by simulation for different scan speeds on three different planes for power of 1250 W.

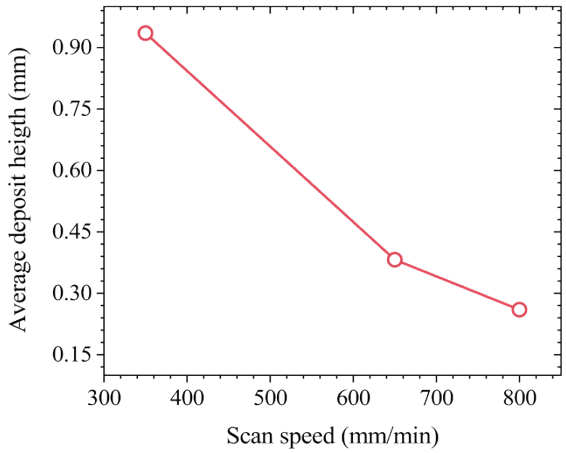

Figure 24: Deposit heights for different scan speeds.

2.5.2 Deposition of multi-track on single layer: Effect of power

Impact of three powers on the fusion characteristics and deposit height were assessed for a hatch spacing of 0.9 mm. The cross-section of the deposits corresponding to each power is provided in Figure 25. It is noteworthy that the fusion of different tracks gets weaker with decrease in power. The number of grooves present in the deposit generated by 850 W is higher than the deposit with power 1050 and 1250 W indicating the onset of lack of fusion. It is projected that the powers lower than 850 W for the same scan speed and hatch spacing is expected to show lack of fusion and not recommended for building C103 parts with scan speed above 800 mm/min and hatch spacing below 0.9 mm. The height of the deposit for different powers are provided in Figure 26. The variation of height of the deposit is negligible and can assumed to be agnostic of the laser power and only a strong function of scanner speed.

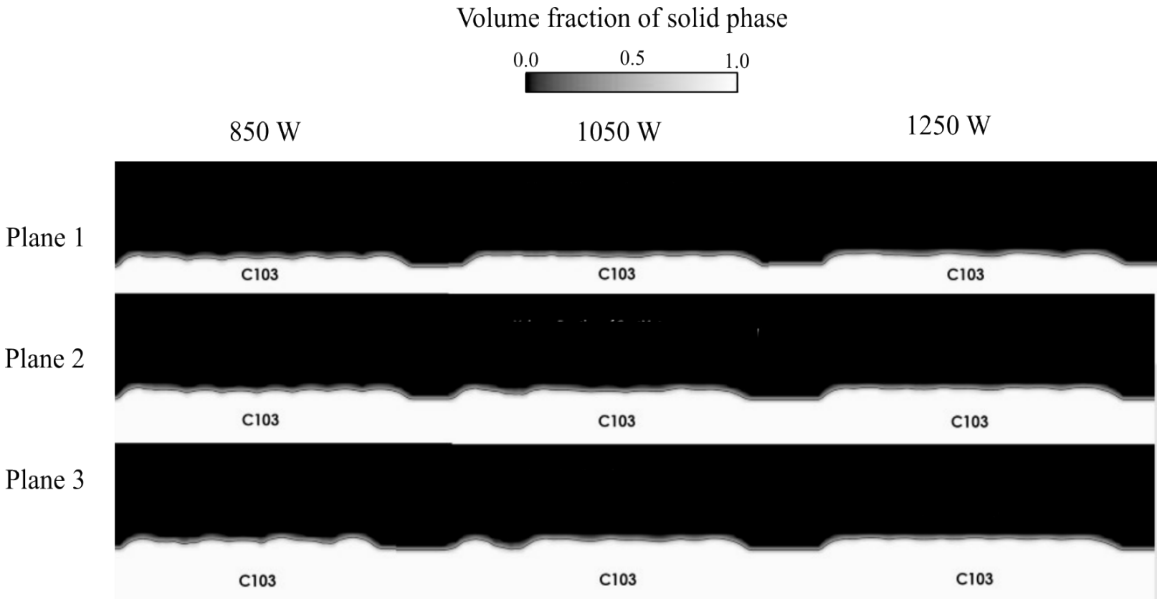

Figure 25: Deposit geometry predicted by simulation for different laser powers for scan speed 800 mm/min and hatch spacing = 0.9 mm.

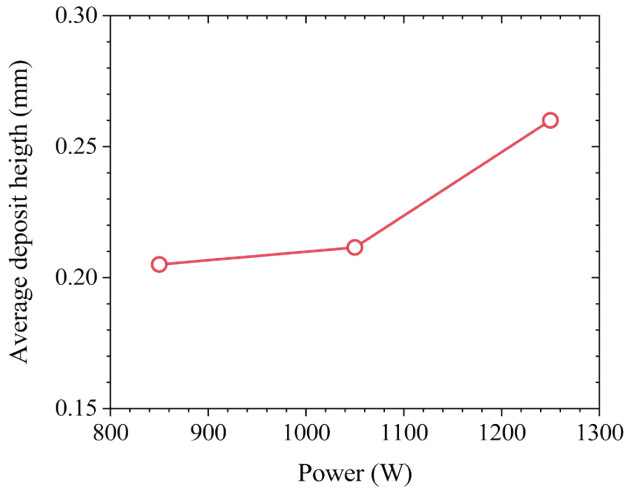

Figure 26: Average deposit height predicted by the eight-track simulation for various values of laser power.

2.5.3 Deposition of multi-track on single layer: Effect of hatch spacing

Hatch spacing is the distance covered by the scanner when it moves between adjacent tracks. Hatch spacing is a crucial parameter which is used to control the lateral fusion and height of the tracks. The deposit cross-sections for hatch spacings, 0.72 mm, 0.9 mm, 1.1 mm and 1.3 mm at a fixed laser power of 1250 W and scan speed of 650 mm/min are provided in Figure 27. It can be observed that the lateral fusion decreases progressively with increasing hatch spacing and can be seen that there is no lateral fusion for hatch spacing 1.3 mm. It can be concluded that to achieve a reasonable lateral fusion between C103 tracks for this power and scan speed, the hatch spacing used should be less than 1.1 mm. The height of the deposit progressively

increases with decrease in hatch spacing due to the overlap of deposits in the adjacent tracks when the hatch spacing is small. The measured height variation of the deposit with hatch spacing provided in Figure 28 verifies this conclusion.

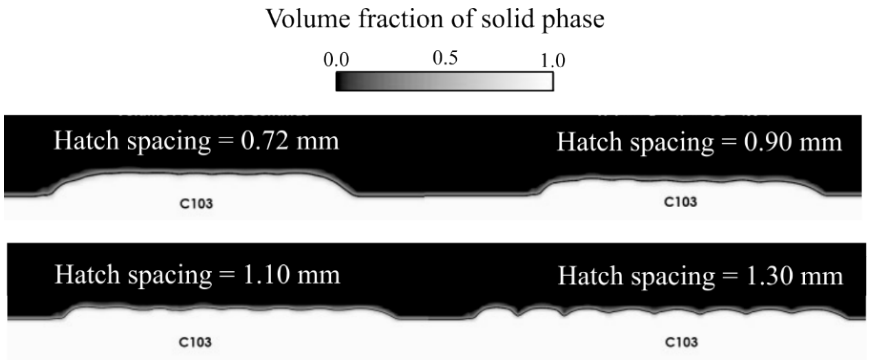

Figure 27: Deposits for different hatch spacings for power =1250 W and scan speed = 650 mm/min.

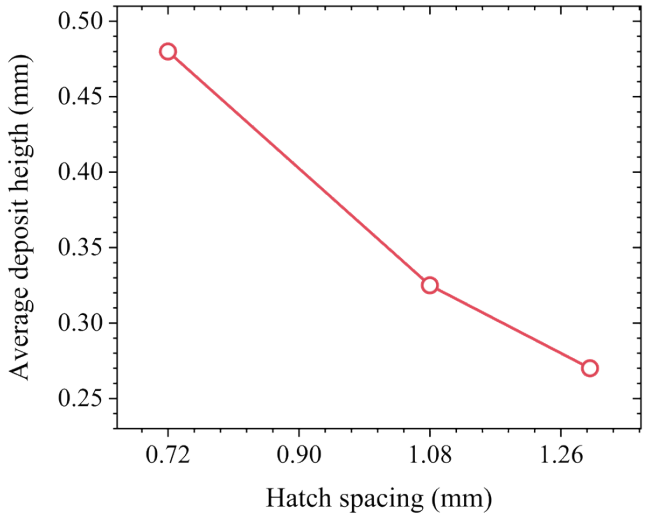

Figure 28: Deposit height for different hatch spacings

2.5.4 Deposition of multi-layer and multi-track: Effect of hatch spacing

Simulations were performed for 4 tracks and 3 overlapping layers of deposit to gain knowledge of lateral fusion between multiple layers of the deposit formed on adjacent tracks and assess the potential of the model to predict large scale defects visible with naked eyes that is formed during the building of the deposit. Figure 29 shows the cross-section of the deposit for hatch spacings: 0.9 mm, 1.1 mm and 1.3 mm for laser power = 1050 W and scan speed = 650 mm/min. It appears that the fusion between tracks is reasonable till a hatch spacing of 1.1 mm and there is a lack of fusion for hatch spacing 1.3 mm, as observed for multi-track single layer deposits. The non-uniformity of the height of the deposit in the lateral direction for different tracks is glaring for hatch spacings 0.9 and 1.1 mm, as compared to the single layer multi-track deposits for the same. In these multi-layer simulations, the upward motion of the scanner at the completion of each layer is not accounted, perhaps this non-uniformity in the height can be related to the lack of scanner

motion vertically during the layer building, as real-life scanners account for this offset. Non-uniformity in the height is less pronounced for hatch spacing 1.3 mm.

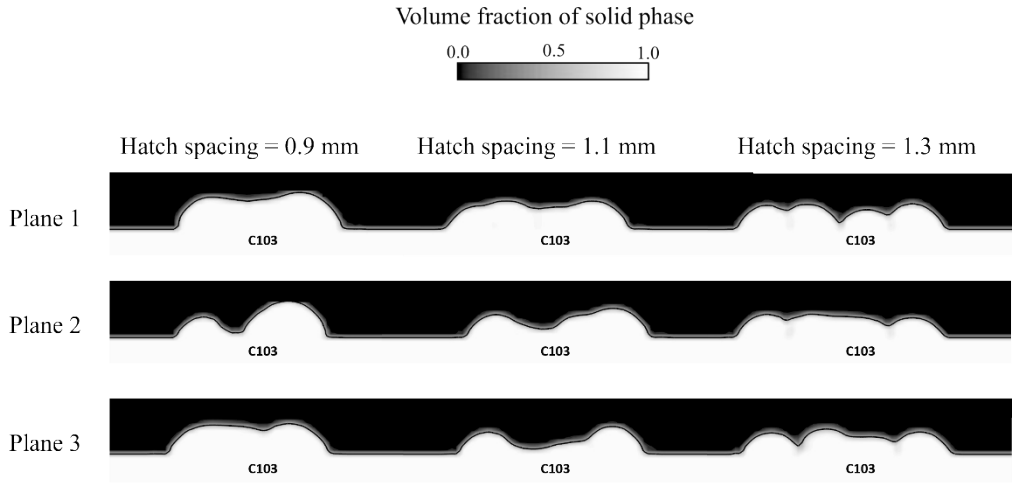

Figure 29: Deposits for different hatch spacing for 4 track 3 layers, power =1050 W and scan speed = 650 mm/min

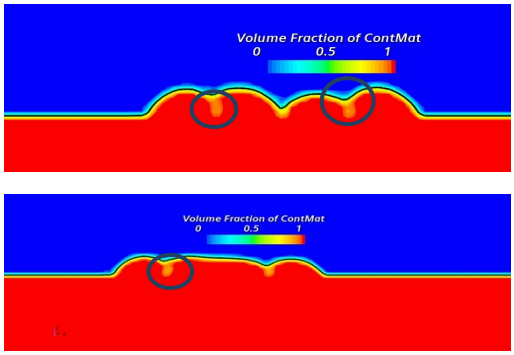

Figure 30: Defects captured through simulations.

The ability of the simulation model to capture the defects such as lack of fusion porosity were unclear in the single layer simulations, however, it is remarkable to note that for multi-layer simulations the simulation model is able to partially capture the holes appearing because of lack of fusion as circled in Figure 30. The numerical diffusion of volume fraction appears to fill this hole as the time progresses, with accurate resolution of the numerical diffusion it is anticipated that this model will have the capability to predict large scale defects like lack of fusion porosity appearing in multi-track-multi-layer DED simulations. The future work will involve investigating this capability of the model and extend it to more complex multi-track-multi-layer simulations to guide defect free building of parts using DED with materials not just limited to C103 studied in this work.

2.6 ESTABLISHEMENT OF PROCESS MAP

2.6.1 Process map for defect detection

The samples printed by CCAM shown in Table 3 were used to establish relationships between defect formation and process variables. To create the process map based on the relationships, the observed defects are first categorized in three distinct categories: 1) lack of fusion (LOF), 2) keyhole, 3) defect-free. The builds with gas porosity were excluded from consideration because gas porosity can originate from trapped

gases within the powder particles or from gases associated with shielding gas, which cannot be simulated in the current version of model. Moreover, the samples with LOF at the interface between Ti-substrate and C103 deposit were not considered in the process map because the simulation is limited to a single material. Therefore, the remaining 21 out of 38 builds were used to construct the process map. Figure 31 shows the established process map of C103 as a function of line energy density (LED) and mass fed per unit length (MFL). The equations used to calculate LED and MFL are given in Eqns.12 and 13. In Figure 31, three regions are identified as keyhole (purple), LOF (red), and defect-free (green). The defect-free builds are found at the low-value regime for both LED and MFL, whereas keyhole defects occur in the high-value regime. Interestingly, LOF defects are widely spread throughout the middle-value regime, specifically in the ranges of 0.0266 to 0.055 g/mm and 77.5 to 83.0 J/mm.

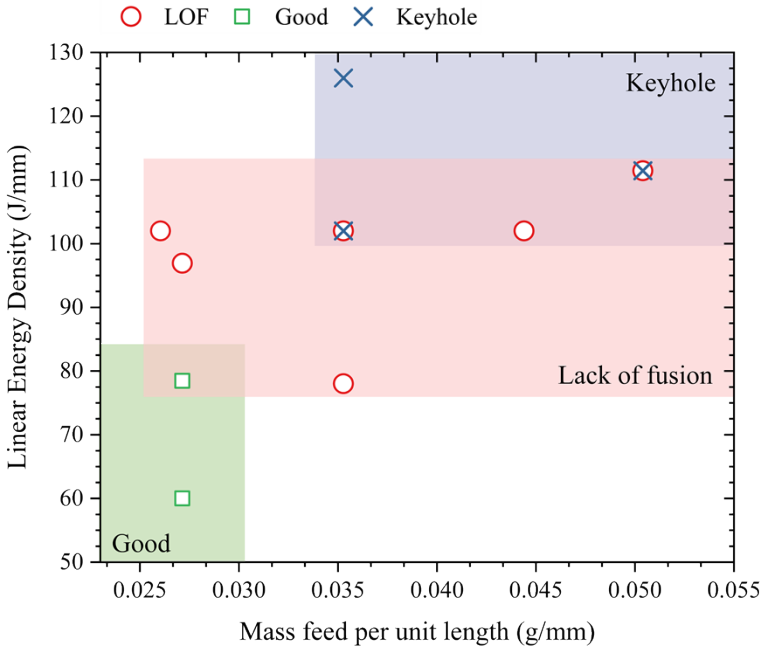

Figure 31: Processing map of C103 demonstrating three regimes: lack of fusion, defect-free (good), and keyhole.

$$\text{LED} = \frac{\text{Laser Power (W)}}{\text{Scan speed (mm/s)}} \tag{12}$$

$$\text{MFL} = \frac{\text{Powder mass flow rate (g/s)}}{\text{Scan speed (mm/s)}} \tag{13}$$

The process map using power (P) and scan speed (V) represents direct control variables in the DED machine and so is more commonly used in the DED process. A P-V process map for the C103 builds is plotted using various combinations of powers (650W, 850W, and 1050W) and scan speeds (350 mm/min, 500 mm/min, and 650 mm/min), while maintaining constant mass flow rate of 0.294 g/min and a stand-off distance of 156 mm in Figure 32. The variations of mass flow rate and a stand-off distance were not considered in this P-V process map, reducing the number of builds to eight. Based on the defect analysis with the optically measured YZ cross-sections in Figure 29 and appendix, the process map is plotted in three types of defects: 1) LOF, 2) keyhole, and 3) defect-free (good). The keyhole defects are found at high-power and low-speed regime corresponding to high LED in Figure 31, whereas defect-free is found at high-speed and low-power regime corresponding to low LED. LOF defects are mostly found in the diagonal regime which corresponds to the middle-value regime in Figure 31. Interestingly, the keyhole defects are found at P/V ratio values, labeled in Figure 32, greater than 2.0, while defect-free builds are found at P/V ratio values around 1.0. The

LOF is found at P/V ratio values between 1.0 and 2.0. Notice that the LOF is also found at 1.3, implying that it can be a threshold value. LOF seems to be more sensitive to scan speed than power.

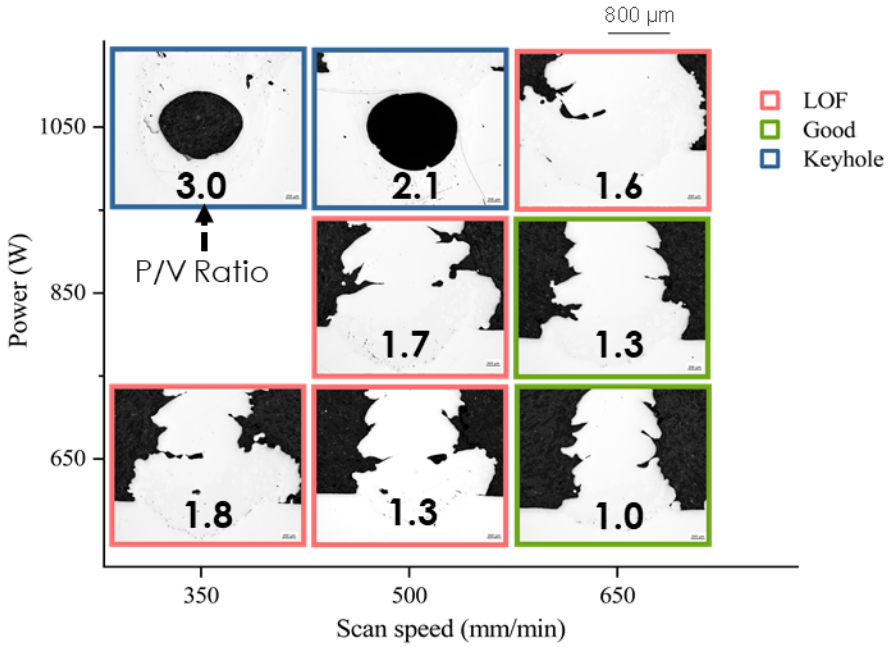

Figure 32: Process map using power and scan speed variable included defect images from an optical microscope.

2.6.2 Process map for geometric precision

The process maps utilizing P, V, and hatch spacing variables are established to understand the effect of the process parameters on deposit topology. To determine the relationships between these variables and deposit geometry, we used the results of the Star-CCM+ simulations from section 2.5 to create the process maps, which involved eight-tracks in a single layer. The deposit geometry has been characterized in terms of three quantities: 1) deposit height (H), 2) width (W), and surface roughness (Ra).

Error! Reference source not found.3 displays the process maps showing the effect of P, V, and hatch spacing on deposit height. In Figure 33(a), the deposit height decreases with an increase in the scan speed. The effect of power on the change in deposit height is stronger at the lower scan speed than at the higher speed. For instance, the deposit height increases at 400 mm/min by 150 µm from 650 µm at 900 W, 750 µm at 1100 W to 800 µm 1200 W, while the increase at 700 mm/min is by 100 µm from 250 µm at 900 W to 350 µm at 1200 W. It is 50% larger increase at the lower scan speed. It can be attributed to the increase of catchment efficiency. Higher power at lower speed effectively widens the melt pool resulting in increase of catchment efficiency, whereas higher power at higher speed is less effective to widen the melt pool due to lowered energy input into the melt pool. The effect of hatch spacing on the deposit height in Figure 33(b) is less significant than the change caused by scan speed in Figure 33(a). The height increase occurs when changing the hatch spacing from 1.3 mm to 0.9 mm leading to an increase from 210 µm to 360 µm, while the change in scan speed results in a larger increase from 210 µm to 850 µm.

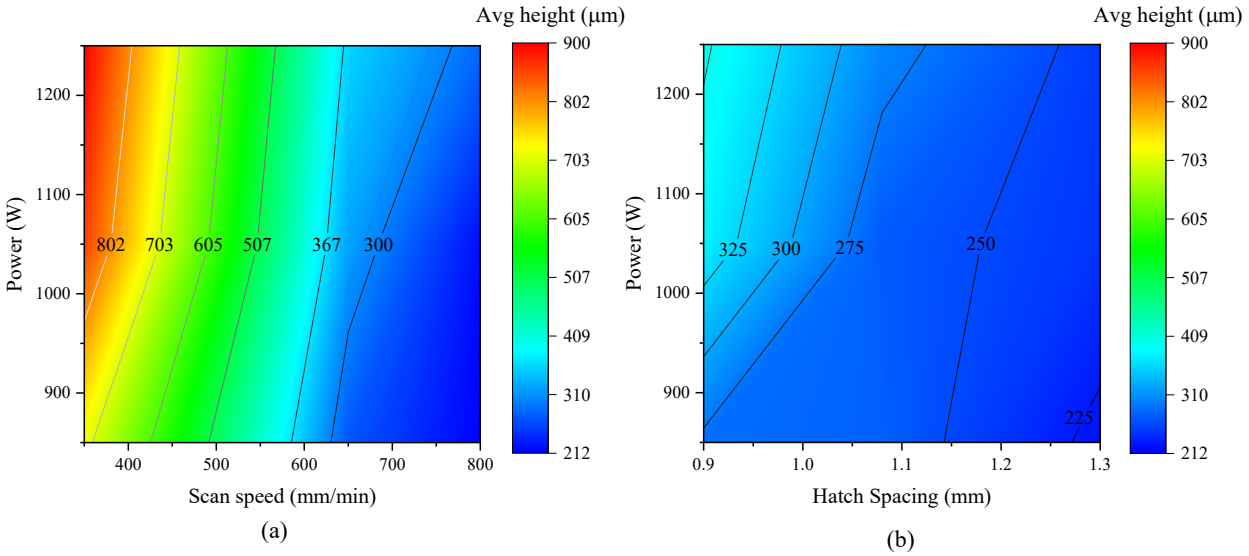

Figure 33: Process maps showing the effect of P, V, and hatch spacing on deposit height (a) Power and scan speed relationship for a hatch spacing of 0.9 mm (b) Power and hatch spacing relationship for a scan speed of 650.

Figure 34 shows the process maps showing the effect of P, V, and hatch spacing on surface roughness Ra. In Figure 34(a), Ra decreases from 35 µm to 20 µm at the speed of 600 mm/min with increase in power from 900 W to 1200 W, while the roughness decreases from 25 µm to 20 µm with increase of speed from 400 mm/min to 800 mm/min at the power of 1050 W. It shows that scan speed has a minor impact on the surface roughness. More noticeable changes in surface roughness were found in Figure 34(b) when examining hatch spacing. Ra increases from 27 µm to 57 µm with increase in hatch spacing from 0.9 mm to 1.1 mm at the power of 1050 W. The change of 30 µm is twice larger change of 15 µm for the power in Figure 31(a). It indicates that the hatch spacing has a stronger impact than scan peed on surface roughness.

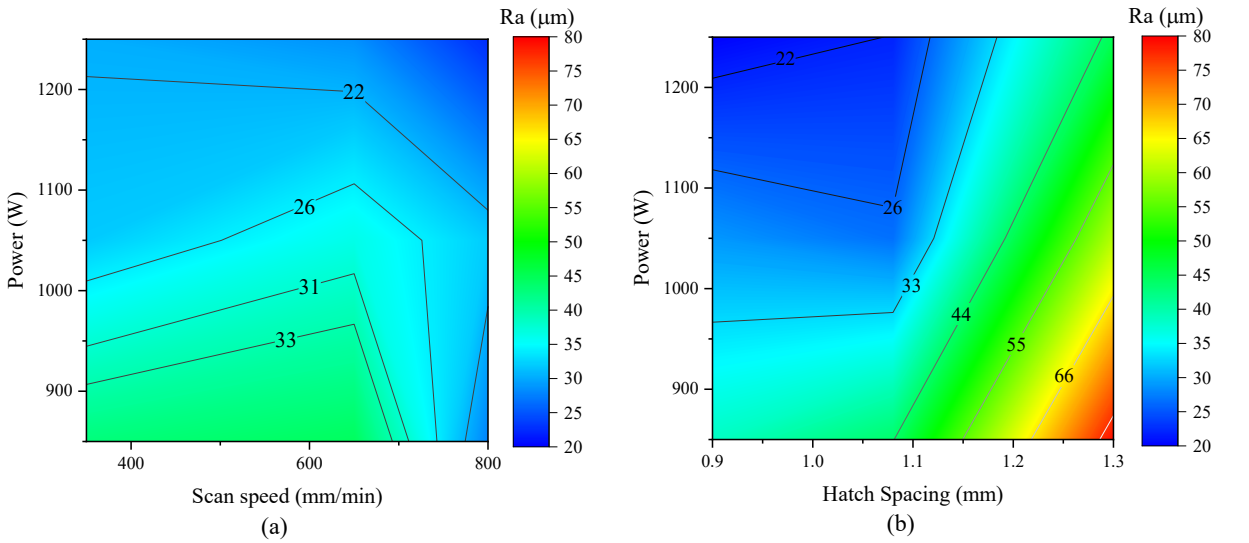

Figure 34: Process map for surface roughness (a) Power versus scan speed for hatch spacing = 0.9 mm (b) Power versus hatch spacing for scan speed = 650 mm/min.

Figure 35 illustrates the process maps showing the effect of P, V, and hatch spacing on deposit width. At lower P-V regime ranging from 850 W to 1050 W in power and 350 mm/min to 750 mm/min, the width variability is insignificant. However, it becomes relatively large as it moves to upper-right corner in the higher P-V regime. A similar trend is observed for hatch spacing. With small width change in the lower P-V regime and relatively large changes in the higher P-hatch spacing regime. This suggests that the width changes are less sensitive at lower P-V levels at smaller hatch spacing.

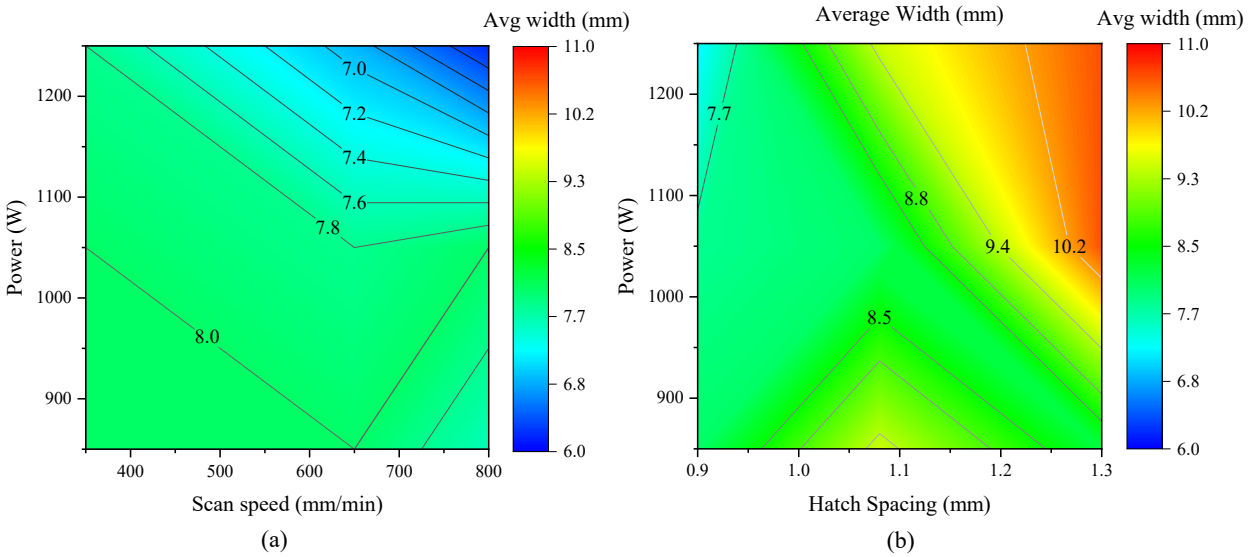

Figure 35: Process map for width (a) Power versus scan speed for hatch spacing = 0.9 mm (b) Power versus hatch spacing for scan speed = 650 mm/min.

The process maps in Figures 33 to 35 illustrated the individual relationships between process parameters and deposit geometries. In most cases, it is important to understand how individual parameters collectively influence broad geometrical changes to find optimal combination of process parameters. Figure 36 shows the combined process map that includes surface roughness, deposit height, and width, and it highlights the presence of a sweet spot among these parameters. Figure 36(a) shows the P-V relationship and Figure 36(b) shows the P-Hatch spacing relationship in relation to changes in deposit geometries.

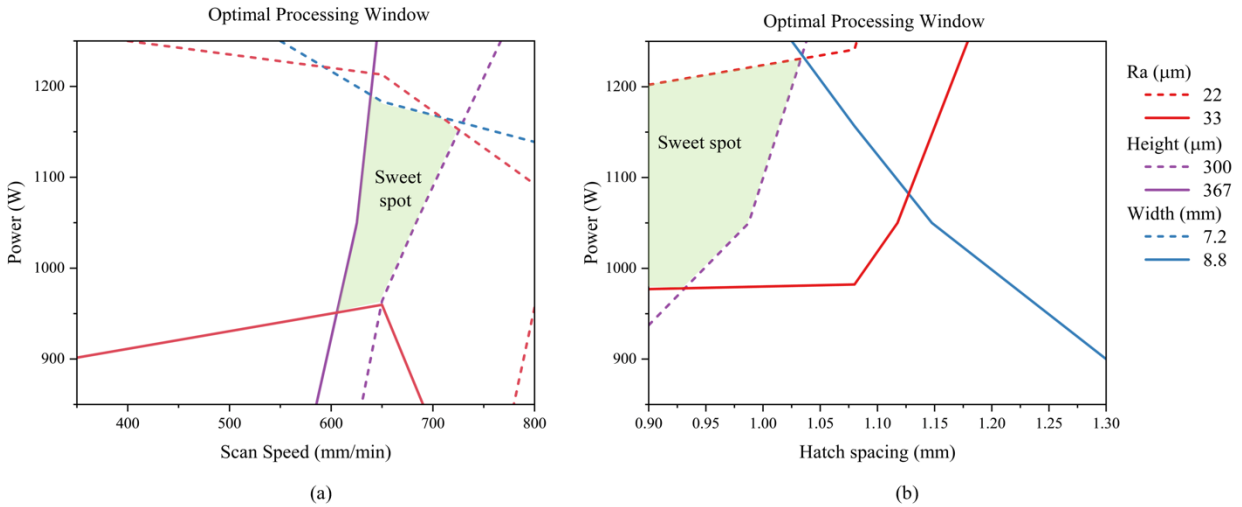

Figure 36: Optimal processing window generated for the C103 alloy using: (a) power-scan speed map at the hatch spacing value of 0.9 mm (b) power-hatch spacing process map at the constant scan speed of 650 mm/min.

In Figure 36, the solid and dashed lines represent the upper and lower limit of surface roughness, height, and width. The upper and lower limit of surface roughness are selected as 33 μm and 22 μm, respectively. This choice is based on the consideration that maintaining the surface roughness less than 10.0% of the deposit height can provide production benefits in production time when surface machining is required to improve fatigue life. The upper and lower limits of the deposit height and width are 367 mm and 300 mm and 8.0 mm and 7.7 mm, respectively. The limits are chosen by ± 10% of the desired deposit height and width. The combined upper and lower limits of each criteria present an optimized range, namely sweet spot in green color, for the power and scan speed at a constant hatch spacing of 0.9 mm in Figure 36(a). The optimal range of process parameters are found in the middle regime of the process map, where scan speed ranging from 600 mm/min to 700 mm/min, and powers ranging from 950 W to 1150 W, are used. Figure 36(b) shows the process map for the power and hatch spacing at a constant scan speed of 650 mm/min. The optimal range of process parameters are found in the upper-left corner, where hatch spacing ranging from 0.9 mm to 1.025 mm, and powers ranging from 980 W to 1250 W, are used. Considering both process maps in Figure 36(a) and (b), the recommended minimum laser power is 900 W and maximum scan speed of 700 mm/min at hatch spacing of 0.9 mm. If the hatch spacing goes beyond 1.05 mm, the deposit height decreases, while the surface roughness starts to excess the upper limit of 33 μm. Larger hatch spacing can reduce production time due to a smaller number of tracks in a given size range. Nevertheless, the trade-off involves an increase in surface roughness. Consequently, it is advisable to avoid excessively large hatch spacing.

2.7 MODELING OF MICROSTRUCTURE

EBSD maps of the builds 7, 8, and 9 in Table 3 are shown in Figure 34. The powers are varied from 650 W, 850W, and 1050 W in the builds while keeping other parameters constant. All three builds exhibit a mixture of equiaxed grains at the periphery and columnar grains in the interior. A gradual transition of grain orientations from <110> green color in Figure 37(a) to <100> red color in Figure 34(c), is observed with an increase in power from 650 W to 1050 W.

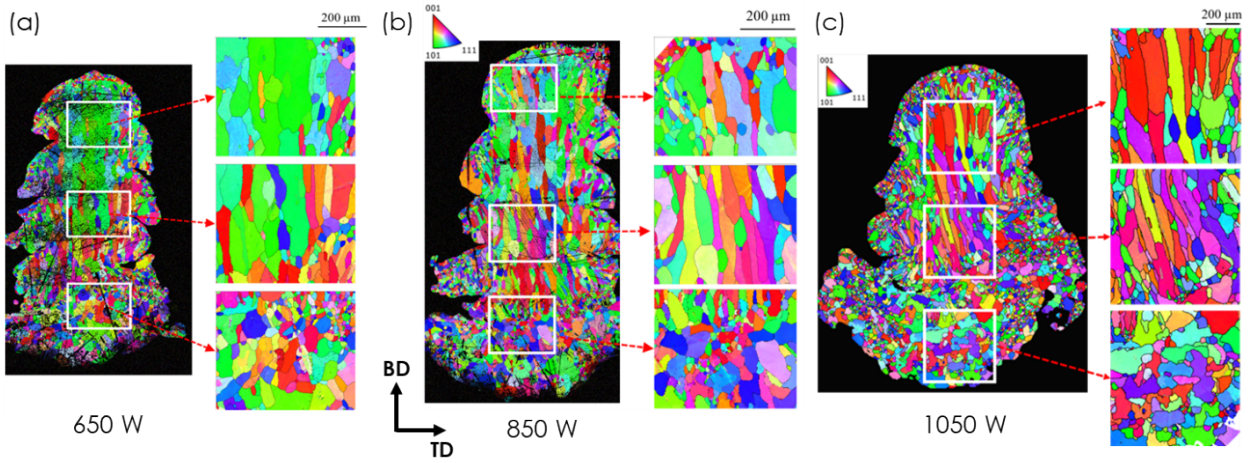

Figure 37: Variations of microstructure at different laser beam power of (a) 650 W, (b) 850 W, and 1050 W. Mixture of equiaxed grains at the periphery and columnar grains in the interior.

The microstructure simulation was performed for a build with 850 W using cellular automata finite element (CAFE) model in Figure 38 [48]. Ten layers were simulated, but only nine layers are compared to the EBSD microstructure in Figure 38(b). The model predicts columnar grains and the distinct layer separations marked as black dashed lines in the build shown in Figure 38(c), which are comparable to the measured microstructure.

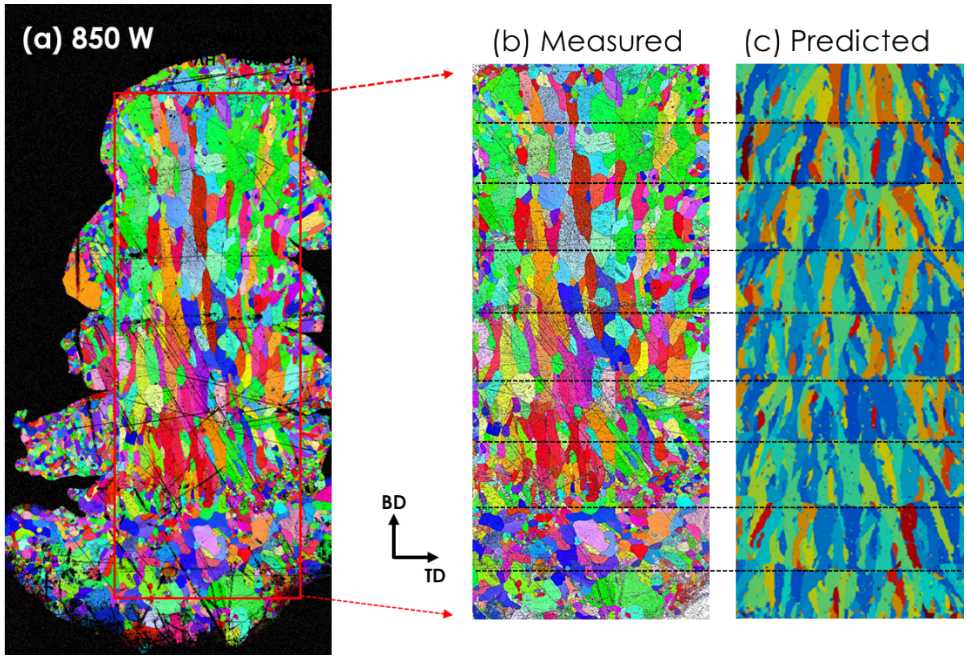

Figure 38: Comparison of microstructure simulation to the measured microstructure at 850 W. (a) the predicted layer separations marked black dashed lines are comparable to (b) the measured microstructure.

The microstructure model was used to investigate the effect of hatching spacing on microstructure in Figure 36. Five hatch spacing variables were chosen, based on the initial conditions (i.e., 460 W, 1300 mm/min) given in Table 2. The layer height of 210 µm and hatch spacing of 333 µm are obtained from the experiment in section 2.4.2, while others are adjusted by approximately 33 µm each: 299 µm, 333 µm, 366 µm, 399

μm, and 499 μm. With an increase of hatch spacing, the number of tracks reduces from six at 299 μm to four at 499 μm within 1700 μm deposit width. This indicates that a decrease in hatch spacing may lead to an increase in printing time. Notice that the microstructure at the overlapped region between tracks marked in red dashed box was chevron-like structure in Figure 39(a) growing outward about 45 degrees at 499 μm hatch spacing. The chevron-like microstructure is gradually tilted and merged upward in Figures 39(b)-(d) and consequently aligns vertically along the build direction in Figure 39(e). While it provides informative results, the accuracy of the prediction will need to be validated in the future.

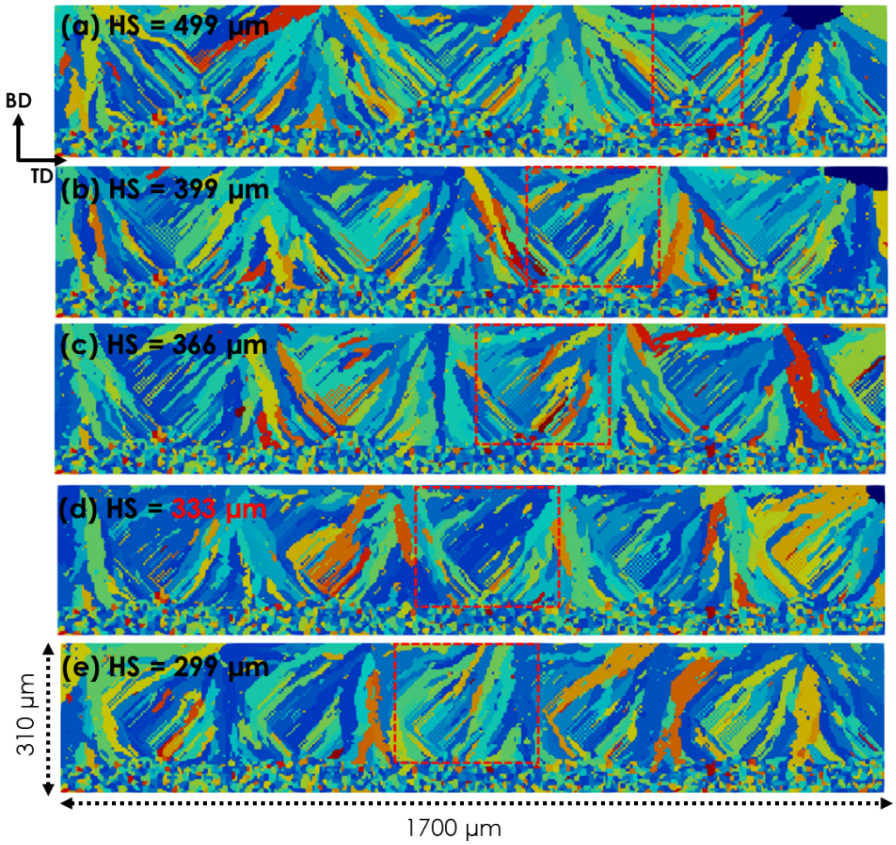

Figure 39: Effect of hatching spacing on microstructure at hatch spacing of (a) 499 μm, (b) 399 μm, (c) 366 μm, (d) 333 μm, and (e) 299 μm. The chevron-like microstructure is gradually tilted and merged upward in (b)-(d) and consequently aligns vertically along the build direction in (e).

3. COMMERCIALIZATION POSSIBILITIES

The developed models and simulation workflow can be incorporated into a software package for modeling of powder DED with refractory alloy of C103. Also, upon successful lab-scale demonstration of the current simulation data, C103 will be used to build a notional component of the turbine blade.

4. PLANS FOR FUTURE COLLABORATION

Based on the current development, the outcomes of modeling and high-fidelity simulation data for C103 acquired through this effort on HPC systems, will be used by both parties for the following:

- Exploring other operating parameters and geometries with increased complexity
- Optimizing process parameters and tool path strategies to ensure part quality
- Linking melt pool simulation to in-situ sensing for closed-loop control

CCAM in collaboration with ORNL is planning to submit a HPC4EI phase 2 proposal to further advance this model and gain more insights on the deposit quality of C103 for different manufacturing conditions. Additionally, ORNL and CCAM will continue to look for any new collaboration opportunities supported through DOE's various program offices.

5. CONCLUSIONS

The project was successfully completed with the goal of advancing the development of the CFD melt pool simulation for powder DED with refractory alloy of C103. Physical interactions among the heat source, material, and manufacturing parameters were carefully corrected in multi-physics simulation Star-CCM+. Then, the results from the experiment and simulation are used to establish process maps for defect detection and geometric precision. Notable accomplishments for this projects are:

- Development of high fidelity CFD melt pool simulation for refractory alloy of C103. To the best of the author's knowledge, there have been few multi-physics melt pool simulations for C103 reported in the literature to date.
- Obtained thermo-physical material properties of C103 from literature and calculated from thermo-dynamic simulation tool are used to validate the simulation accuracy in terms of 1) scan speed, 2) laser power, and 3) hatch spacing with single layer multi-track builds and multi-layer multi-track builds. The predicted dimensions of the deposits are consistent in trend with the measured values.
- The results from the experiments and simulations are used to establish process maps for defect detection and geometric precision. The map found the sweet spot among the process parameters. It indicates that larger hatch spacing can reduce production time due to a smaller number of tracks in a given size range. Nevertheless, the trade-off involves an increase in surface roughness. Consequently, it is advisable to avoid excessively large hatch spacing.
- Microstructure simulation was performed using CAFÉ model to link the melt pool simulation to the microstructure characteristics at various process conditions. The prediction shows a consistency in the grain morphology and growth pattern at defect-free condition.

The technical scope of this work aligns with a larger computational modeling framework aimed at enabling comprehensive simulation of powder DED to facilitate virtual process design and part quality certification. Also, the outcomes of simulations and data for C103 can be used to optimize the process parameters and tool path strategies to ensure the defect-free parts. The CFD melt pool simulation can potentially be integrated into an in-situ sensing system in the future. The integration would enable closed-loop control to provide guidance to both the DED machine and the machine operator. The technology developed in the project supports the optimization of the powder DED process, reduces design lead time, and minimizes rejected parts.

6. REFERENCES

1. Philips, N.R., M. Carl, and N.J. Cunningham, *New Opportunities in Refractory Alloys.* Metallurgical and Materials Transactions A, 2020. **51**: p. 3299-3310.
2. Smallwood, R.E., *Refractory metals and their industrial applications: a symposium*. Vol. 849. 1984: ASTM International.
3. Gradl, P., et al., *Advancement of extreme environment additively manufactured alloys for next generation space propulsion applications.* Acta Astronautica, 2023. **211**: p. 483-497.
4. Mireles, O., et al., *Additive manufacture of refractory alloy C103 for propulsion applications*, in *AIAA Propulsion and Energy 2020 Forum*. 2020. p. 3500.
5. Wojcik, C.C., *Processing, properties and applications of high-temperature niobium alloys.* MRS Online Proceedings Library (OPL), 1993. **322**.
6. Rieth, M., et al., *Recent progress in research on tungsten materials for nuclear fusion applications in Europe.* Journal of Nuclear Materials, 2013. **432**(1-3): p. 482-500.
7. Duan, Z., et al., *Current status of materials development of nuclear fuel cladding tubes for light water reactors.* Nuclear Engineering and Design, 2017. **316**: p. 131-150.
8. Grandin, H.M., S. Berner, and M. Dard, *A review of titanium zirconium (TiZr) alloys for use in endosseous dental implants.* Materials (Basel), 2012. **5**(8): p. 1348-1360.
9. Shinjo, J. and C. Panwisawas, *Chemical species mixing during direct energy deposition of bimetallic systems using titanium and dissimilar refractory metals for repair and biomedical applications.* Additive Manufacturing, 2022. **51**.
10. Griemsmann, T., et al., *Laser-based powder bed fusion of niobium with different build-up rates.* The International Journal of Advanced Manufacturing Technology, 2021. **114**: p. 305-317.
11. Schwartz, N., M. Gresh, and S. Karlik, *Niobium solid electrolytic capacitors.* Journal of The Electrochemical Society, 1961. **108**(8): p. 750.
12. Freeman, Y., *Tantalum and niobium-based capacitors.* Science, Technology, and Applications, 2018.
13. Autler, S.H., E.S. Rosenblum, and K.H. Gooen, *High-field superconductivity in niobium.* Physical Review Letters, 1962. **9**(12): p. 489.
14. Aimone, P. and M. Yang, *Niobium alloys for the chemical process industry.* International Journal of Refractory Metals and Hard Materials, 2018. **71**: p. 335-339.
15. Awasthi, P.D., et al., *Mechanical properties and microstructural characteristics of additively manufactured C103 niobium alloy.* Materials Science and Engineering: A, 2022. **831**.
16. Mastanaiah, P., et al., *An investigation on microstructures and mechanical properties of explosive cladded C103 niobium alloy over C263 nimonic alloy.* Journal of Materials Processing Technology, 2014. **214**(11): p. 2316-2324.
17. Sergi, A., et al., *Powder HIP of pure Nb and C-103 alloy: The influence of powder characteristics on mechanical properties.* International Journal of Refractory Metals and Hard Materials, 2022. **104**.
18. Morales, R., et al., *The Powder Metallurgy Processing of Refractory Metals and Alloys.* JOM, 2003. **55**: p. 20-23.
19. Mireles, O., *Additive Manufacture of Refractory Metals for Aerospace Applications*, in *AIAA Propulsion and Energy 2021 Forum*. 2021. p. 3234.
20. Talignani, A., et al., *A review on additive manufacturing of refractory tungsten and tungsten alloys.* Additive Manufacturing, 2022. **58**.
21. Terrazas, C.A., et al., *Fabrication and characterization of high-purity niobium using electron beam melting additive manufacturing technology.* The International Journal of Advanced Manufacturing Technology, 2016. **84**: p. 1115-1126.

22. Scott, M. and P. Knowlson, *The welding and brazing of the refractory metals niobium, tantalum, molybdenum and tungsten—a review.* Journal of the Less Common Metals, 1963. **5**(3): p. 205-244.
23. Osher, S. and J.A. Sethian, *Fronts propagating with curvature-dependent speed: Algorithms based on Hamilton-Jacobi formulations.* Journal of computational physics 1988. **79**(1): p. 12-49.
24. Hirt, C.W. and B.D. Nichols, *Volume of fluid (VOF) method for the dynamics of free boundaries.* Journal of computational physics, 1981. **39**(1): p. 201-225.
25. Morville, S., et al., *2D longitudinal modeling of heat transfer and fluid flow during multilayered direct laser metal deposition process.* Journal of Laser Applications, 2012. **24**(3).
26. Gan, Z., et al., *Numerical simulation of thermal behavior and multicomponent mass transfer in direct laser deposition of Co-base alloy on steel.* International Journal of Heat and Mass Transfer, 2017. **104**: p. 28-38.
27. Li, C., et al., *Numerical simulation and experimental study of cladding Fe60 on an ASTM 1045 substrate by laser cladding.* Surface and Coatings Technology, 2019. **357**: p. 965-977.
28. Wirth, F. and K. Wegener, *A physical modeling and predictive simulation of the laser cladding process.* Additive Manufacturing, 2018. **22**: p. 307-319.
29. Zhao, J., et al., *Multicomponent multiphase modeling of dissimilar laser cladding process with high-speed steel on medium carbon steel.* International Journal of Heat and Mass Transfer, 2020. **148**.
30. Wei, S., et al., *Comprehensive modeling of transport phenomena in laser hot-wire deposition process.* International Journal of Heat and Mass Transfer, 2018. **125**: p. 1356-1368.
31. Ferreira, R.B., et al., *Numerical simulations of two-phase flow in proton exchange membrane fuel cells using the volume of fluid method – A review.* Journal of Power Sources, 2015. **277**: p. 329-342.
32. Han, L., K. Phatak, and F. Liou, *Modeling of laser cladding with powder injection.* Metallurgical and Materials transactions B, 2004. **35**: p. 1139-1150.
33. Kong, F. and R. Kovacevic, *Modeling of heat transfer and fluid flow in the laser multilayered cladding process.* Metallurgical and materials transactions B, 2010. **41**: p. 1310-1320.
34. Qi, H., J. Mazumder, and H. Ki, *Numerical simulation of heat transfer and fluid flow in coaxial laser cladding process for direct metal deposition.* Journal of applied physics, 2006. **100**(2).
35. Wen, S. and Y.C. Shin, *Modeling of transport phenomena during the coaxial laser direct deposition process.* Journal of Applied Physics, 2010. **108**(4).
36. Lee, Y.S., et al., *Influence of fluid convection on weld pool formation in laser cladding. Weld.* Welding Journal, 2014. **93**(8): p. 292-300.
37. Lee, Y. and D.F. Farson, *Simulation of transport phenomena and melt pool shape for multiple layer additive manufacturing.* Journal of Laser Applications, 2016. **28**(1).
38. Wei, H.L., et al., *Prediction of spatiotemporal variations of deposit profiles and inter-track voids during laser directed energy deposition.* Additive Manufacturing, 2020. **34**.
39. Zhang, Y.M., et al., *Numerical investigation on heat transfer of melt pool and clad generation in directed energy deposition of stainless steel.* International Journal of Thermal Sciences, 2021.
40. Sun, Z., W. Guo, and L. Li, *Numerical modelling of heat transfer, mass transport and microstructure formation in a high deposition rate laser directed energy deposition process.* Additive Manufacturing, 2020. **33**.
41. Ibarra-Medina, J. and A.J. Pinkerton, *A CFD model of the laser, coaxial powder stream and substrate interaction in laser cladding.* Physics Procedia, 2010. **5**: p. 337-346.
42. Wen, S., et al., *Modeling of coaxial powder flow for the laser direct deposition process.* International Journal of Heat and Mass Transfer, 2009. **52**(25-26): p. 5867-5877.
43. Wang, S., et al., *Multi-physics modeling and Gaussian process regression analysis of cladding track geometry for direct energy deposition.* Optics and Lasers in Engineering, 2020. **127**.

44. Bayat, M., et al., *On the role of the powder stream on the heat and fluid flow conditions during Directed Energy Deposition of maraging steel—Multiphysics modeling and experimental validation.* Additive Manufacturing, 2021. **43**.
45. Dalagan, A., *Investigation of Primary Process Parameters for Laser Powder Bed Fusion of High Temperature Alloys through Physical and Virtual Experimentation*. 2022, University of Virginia.
46. Arruzieta, J.I., et al., *Evaluation of the relevance of melt pool dynamics in Laser Material Deposition process modeling.* International Journal of Heat and Mass Transfer, 2017: p. 80 - 91.
47. Chen, X., *Modelling of directed energy deposition processes*. 2013: Missouri University of Science and Technology.
48. Teferra, K. and D.J. Rowenhorst, *Optimizing the cellular automata finite element model for additive manufacturing to simulate large microstructures.* Acta Materialia, 2021. **213**.

7. APPENDIX

A.1 RESULS OF OPTICAL MICROSCOPY

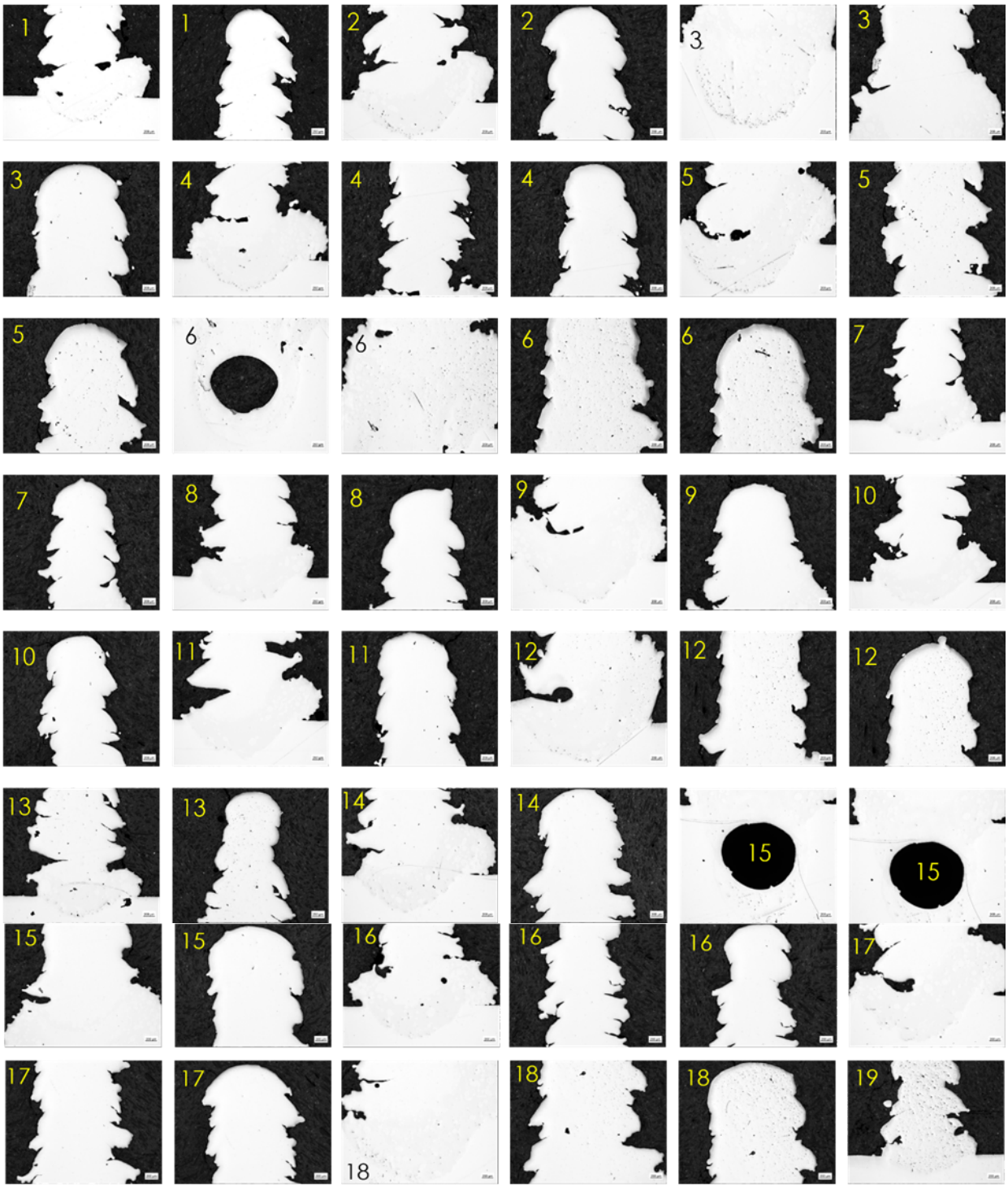


19
20
20
21
21
22
22
23
23
24
24
25
25
26
26
27
27
28
28
28
29
29
29
30
30
30
31
31
31
32
32
32
33
33
33
34
34
34
34
35
35
34
35
35
36
36
36
37
37
37
37
38
38
38